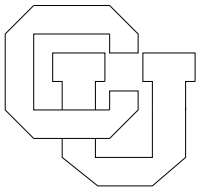

University of Colorado at Denver

An ELLAM Approximation for Advective-Dispersive Transport with Nonlinear Sorption

Matthew W. Farthing, Christopher E. Kees,
Thomas, F. Russel and Cass T. Miller

March, 2004 UCD/CCM Report No. 206

CENTER FOR COMPUTATIONAL MATHEMATICS REPORTS

An ELLAM approximation for advective-dispersive transport with nonlinear sorption

Matthew W. Farthing [a,*], Christopher E. Kees [b], Thomas F. Russell [c,1], Cass T. Miller [a]

[a] *Center for the Integrated Study of the Environment, Department of Environmental Sciences and Engineering, University of North Carolina, Chapel Hill, North Carolina 27599-7431, USA*

[b] *U.S. Army Engineer Research and Development Center, Coastal and Hydraulics Laboratory, 3909 Halls Ferry Road, Vicksburg, MS 39180-6199, USA*

[c] *Department of Mathematics, University of Colorado at Denver, P.O. Box 173364, Campus Box 170, Denver, CO 80217-3364, USA*

Abstract

We consider an Eulerian-Lagrangian localized adjoint method (ELLAM) applied to nonlinear model equations governing solute transport and sorption in porous media. Solute transport in the aqueous phase is modeled by standard advection and hydrodynamic dispersion processes, while sorption is modeled with a nonlinear local equilibrium model. We present our implementation of finite volume ELLAM (FV-ELLAM) and finite element (FE-ELLAM) discretizations to the reactive transport model and evaluate their performance for several test problems containing self-sharpening fronts.

Preprint submitted to Elsevier Science *28 February 2005*

Key words: ELLAM, porous media, Freundlich, contaminant transport

Notation

Roman Letters

C	aqueous phase solute concentration
$\hat{C}$	trial solution
C^b	inflow boundary value for aqueous phase solute concentration
C_e	aqueous phase equilibrium solute concentration
$C^{n+1,m}$	nonlinear solver's current guess for concentration at t^{n+1}
C^*	boundary value at $-\infty$ for traveling wave example
C_*	boundary value at ∞ for traveling wave example
C_L	Riemann problem left state
C_R	Riemann problem right state
D	hydrodynamic dispersion coefficient
K_f	Freundlich sorption capacity coefficient
M	normalized total concentration, $C + \varphi(C)$
$\mathcal{M}^h$	discrete spatial mesh
R_f	retardation factor, $1 + \frac{d\varphi}{dC}$

* Corresponding author
Email addresses: matthew_farthing@unc.edu (Matthew W. Farthing),
Christopher.E.Kees@erdc.usace.army.mil (Christopher E. Kees),
trussell@nsf.gov (Thomas F. Russell), casey_miller@unc.edu (Cass T. Miller).
[1] current address: Division of Mathematical Sciences, National Science Foundation, 4201 Wilson Blvd. Arlington, VA 22230, USA

T	extent of temporal domain
W	FV-ELLAM approximate test function
X	parameterization for tracking along solution characteristics (see eqns (27) and (28))
X_a	parameterization for tracking along adjoint characteristics (see eqns (25) and (26))
c_{fr}	wave speed cutoff for FT tracking
$d_{1-\epsilon}$	front width in traveling wave example
f	continuous solute sources and sinks
n	outward unit normal on $\partial\Omega$
$n_e + 1$	number of nodes in $\mathcal{M}^h$
n_f	exponent in Freundlich sorption isotherm
n_q	number of integration points
n_{st}	number of tracking substeps
q^b	total flux boundary value on inflow boundary
r_q	numerical integration weight
t	time coordinate
$t^{n,k}$	tracking time level, $t^{n,k} = t^n + k\Delta\tau$
v	mean pore velocity
w	test function
x	space coordinate
x_L	left end of spatial domain
x_R	right end of spatial domain
$x_{i+1/2}$	FV-ELLAM cell boundary, $(x_i + x_{i+1})/2$
x_s^{n+1}	intersection of shock at time level $n+1$ in Riemann example
x_q	numerical integration point

Greek Letters

Δt^{n+1}	time step, $t^{n+1} - t^n$.
$\Delta\tau$	tracking time step
Δx_i	spatial increment, $x_{i+1/2} - x_{i-1/2}$
$\Delta x_{i+1/2}$	spatial increment, $x_{i+1} - x_i$
$\overline{\Delta x}$	support parameter for W_i, $\overline{\Delta x} = \Delta x/\mathrm{NS}$
Δx_{min}	approximate minimum front resolution required
Γ_O	outflow spatial boundary
Γ_I	inflow spatial boundary
Ω	spatial domain
Ω_i	spatial interval associated with node i
α	wave speed for traveling wave example
$\partial\Omega$	boundary of spatial domain
δ_{fr}	discretization parameter for FT tracking
ϵ	front width parameter for traveling wave example
η	traveling wave coordinate, $\eta = x - \alpha t$
θ	porosity
λ	characteristic speed, v/R_f
λ_a	adjoint equation characteristic speed, $(vC)/[C + \varphi(C)]$
ρ_b	bulk density of the solid phase
σ	shock speed
φ	normalized isotherm, $[\rho_b \omega_e(C)]/\theta$
ψ	piecewise-linear Lagrangian shape function
ω_e	solid phase equilibrium solute mass fraction
ω_f	solid phase solute mass fraction

Subscripts and Superscripts

a	quantity associated with adjoint characteristics (subscript)
i	nodal value (subscript)
j	nodal value (subscript)
m	nonlinear solver iteration level (superscript)
n	time level (superscript)
$\tilde{}$	forward-tracked quantity (superscript)
$*$	backward-tracked quantity (superscript)

Abbreviations

BE	backward Euler time discretization
BE-S	tracking strategy using BE with $\Delta\tau = \Delta t^{n+1}$
BL	bilinear interpolation in space and time
Cr	Courant number
ELLAM	Eulerian-Lagrangian localized adjoint method
FE-ELLAM	finite element ELLAM
FT	front-tracking method
FV-ELLAM	finite volume ELLAM
MMOC	modified method of characteristics
NS	FV-ELLAM parameter for approximate test function, W
NT	number of composite trapezoidal rule intervals (in time) along inflow boundary
Pe	mesh Peclet number
RK2	second-order explicit Runge-Kutta time discretization
RK2-S	tracking strategy using RK2 with $\Delta\tau = \Delta t^{n+1}$

RK2-BL	tracking strategy combining RK2 with BL
RK2-FT	tracking strategy combining RK2 with FT
SSIP	strategic spatial integration point
STIP	strategic temporal integration point

1 Introduction

Much effort has been devoted to the numerical simulation of contaminant transport processes in the subsurface over the last few decades [5, 28]. Despite significant advancements, accurate and efficient simulation remains a challenge in many cases, particularly for advective-dominated problems involving nonlinear chemical reactions and mass transfer [16, 20]. Characteristic-based methods such as Lagrange-Galerkin discretizations [4, 29], the modified method of characteristics (MMOC) [13], and ELLAMs [9] have been applied to a wide range of transport problems. These methods typically combine a Lagrangian approach for advection with Eulerian discretizations for other transport processes such as physical dispersion. Since they rely on a Lagrangian framework for advection, characteristic-based methods are often able to provide sharp resolution of fronts on relatively coarse grids while avoiding stability restrictions on the Courant number commonly found in Eulerian methods [14]. Among characteristic-based methods, ELLAM approaches have the additional advantages that they provide mass conservation and incorporate boundary conditions in a systematic way [31].

A general review of characteristic-based methods and ELLAM approaches in particular is beyond the scope of this work. We refer the reader instead to Russell and Celia [31] and Ewing and Wang [14]. In brief, ELLAM dis-

cretizations for linear transport are mature. A number of practical two- and three-dimensional problems have been solved successfully using ELLAM approximations [7, 8, 18, 40], and an FV-ELLAM option has been incorporated in the USGS MOC3D code [32]. ELLAM approaches have also been considered for several nonlinear problems including two-phase flow via the Buckley-Leverett equation with capillary pressure [11], and advective-dispersive transport with biodegradation [6, 35, 41]. Initial work has been reported for general compositional formulations of multiphase flow [42] as well. However, ELLAM approaches for nonlinear problems are less advanced than their linear counterparts. Nonlinear transport problems introduce several additional complexities. Solution fronts can, for example, be self-sharpening (shocks) rather than contact discontinuities, and reaction terms can be sensitive to overshoot and undershoot in the solution [27]. To realize the same level of success that has been achieved for linear problems with nonlinear reactive transport, more work is needed to develop approaches within the ELLAM framework that can effectively maintain accurate resolution for large time steps and mass conservation in the presence of these additional challenges [8].

Previous ELLAM approaches for nonlinear reactive transport have considered contaminant biodegradation modeled by Monod kinetics in both fully coupled [35, 41] and operator-split frameworks [6]. Within an operator splitting context, ELLAM methodologies can be carried over directly to the linear transport equation. The fully coupled formulations account for the reaction terms in the ELLAM test functions. The methods of Wang et al. [41] and Våg et al. [35] are based on linearizing the Monod reaction terms and defining ELLAM test functions to increase or decrease along characteristics, as with solution to problems involving transport and linear decay. Various techniques

are then necessary to account for the error arising from the linearization. However, the basic methods for tracking information along characteristics in the corresponding linear transport problem can still be used [35, 41]. For many nonlinear problems of interest, this approach will not be effective.

Several Eulerian-Lagrangian discretizations including characteristic Galerkin [12] and Lagrange-Galerkin methods [4, 23, 24] have been applied to one-dimensional advective-dispersive transport with both equilibrium and non-equilibrium sorption in non-divergence form. ELLAM formulations that are applied directly to the divergence form of the underlying transport problem have advantages in handling of boundary conditions and ensuring conservation of mass [31]. In addition, previous Eulerian-Lagrangian methods accounted for Lagrangian aspects of their discretization using characteristics from the hyperbolic portion of the original transport equation [4, 23, 24]. While tracking these characteristic curves in space and time details the propagation of solution values, characteristics become nonunique in the presence of a shock [27]. A potential, under-explored solution to this problem is to track characteristics for the ELLAM test functions, which satisfy a *linear* adjoint equation, and so avoid the difficulties associated with tracking characteristics of the original transport equation when problems exhibit self-sharpening fronts.

The overall goal of this work is to advance ELLAM approaches for the solution of a common class of nonlinear transport problems using approaches that conserve mass, are able to resolve self-sharpening fronts, and accommodate boundary conditions naturally. The specific objectives of this work are: (1) to summarize a common nonlinear transport model that poses challenges for traditional ELLAM approaches; (2) to detail mass conservative FE-ELLAM and FV-ELLAM approximation of the nonlinear problem; (3) to formulate

alternative approaches for approximating the nonlinear tracking along characteristics; and (4) to compare the various ELLAM approaches for a range of test problems and spatial and temporal step sizes.

2 Model Formulation

We sought a nonlinear model problem that embodied the challenges of sharp-front resolution, mass conservation, and the flexible and accurate accommodation of boundary conditions, which were highlighted above as open issues. A common nonlinear model that meets these criteria is advective-dispersive transport in the presence of nonlinear, local-equilibrium sorption to a fixed solid phase, which is described by the Freundlich equilibrium model [15, 20]. This model is relevant because it may be used as at least a first-cut approximation for the transport of a large number of neutral hydrophobic solutes through porous media that include soils, sediments, and aquifer materials [2, 5]. A weakness in this model is that it assumes that the solute achieves equilibrium locally, or rapidly in comparison to the rate of transport through the system—an assumption that may not hold for many frequently encountered situations [5].

Because our focus is on methods development, we examine a one-dimensional form of this model given by

$$\frac{\partial C}{\partial t} + \frac{\rho_b}{\theta}\frac{\partial \omega_f}{\partial t} + \frac{\partial (vC)}{\partial x} - \frac{\partial}{\partial x}\left(D\frac{\partial C}{\partial x}\right) = f(x,t) \text{ in } \Omega \times [0,T] \tag{1}$$

$$\omega_f = \omega_e(C) \tag{2}$$

where C is the aqueous-phase solute concentration, t is time, ρ_b is the bulk

density of the solid phase, θ is the porosity, ω_f is the solid-phase solute mass fraction, v is the mean pore velocity, x is the spatial coordinate, D is the hydrodynamic dispersion coefficient, f represents a solute source or sink, Ω is the spatial domain, $[0, T]$ is the temporal domain, and ω_e is the solid-phase solute mass fraction in equilibrium with the fluid-phase equilibrium solute concentration C_e. The solid-phase equilibrium solute mass fraction is described using the Freundlich equilibrium model

$$\omega_e = K_f C^{n_f} \tag{3}$$

where K_f is a sorption capacity coefficient, and the exponent n_f is a measure of the sorption intensity.

The initial aqueous-phase solute concentration and solid-phase solute mass fraction are denoted by $C(x, t = 0) = C^0(x)$ and $\omega_f(x, t = 0) = \omega_e(C^0)$. ELLAM formulations naturally incorporate a range of boundary conditions [31]. However, we restrict ourselves to a total flux condition on the inflow boundary and zero dispersive flux along the outflow boundary for simplicity

$$\begin{aligned} \left(vC - D\frac{\partial C}{\partial x} \right) \cdot n &= q^b(x,t) \text{ for } x \in \Gamma_I, \\ \frac{\partial C}{\partial x} \cdot n &= 0 \text{ for } x \in \Gamma_O \end{aligned} \tag{4}$$

where $\Gamma_I \cup \Gamma_O = \partial\Omega$, $\Gamma_I \cap \Gamma_O = \emptyset$, and $\partial\Omega$ is the boundary of Ω. n is the outward unit normal on $\partial\Omega$ with $v \cdot n < 0$ on Γ_I and $v \cdot n \geq 0$ on Γ_O. In the the one-dimensional problems we consider here, Γ_I and Γ_O each consist of a single point.

Following traditional ELLAM approaches [9, 31] and our preliminary efforts on this model problem [15], we rewrite eqn (1) in a slightly more general form

for convenience:

$$\frac{\partial M(C)}{\partial t} + \frac{\partial}{\partial x}\left(vC - D\frac{\partial C}{\partial x}\right) = f(x,t) \text{ in } \Omega \times [0,T] \tag{5}$$
$$M(C) = C + \frac{\rho_b}{\theta}\omega_e(C) = C + \varphi(C)$$

We next multiply eqn (5) by a test function $w(x,t)$, integrate over $\Omega \times [0,T]$ and expand to obtain

$$\int_\Omega \int_0^T \left(\frac{\partial [M(C)w]}{\partial t} - M(C)\frac{\partial w}{\partial t}\right) \mathrm{d}t\,\mathrm{d}x + \int_0^T \int_\Omega \frac{\partial}{\partial x}\left[w\left(vC - D\frac{\partial C}{\partial x}\right)\right] \mathrm{d}x\,\mathrm{d}t$$
$$- \int_0^T \int_\Omega \left(vC\frac{\partial w}{\partial x} - D\frac{\partial C}{\partial x}\frac{\partial w}{\partial x}\right) \mathrm{d}x\,\mathrm{d}t = \int_0^T \int_\Omega fw\,\mathrm{d}x\,\mathrm{d}t \tag{6}$$

After reordering terms, we have

$$\int_\Omega \int_0^T \frac{\partial [M(C)w]}{\partial t}\,\mathrm{d}t\,\mathrm{d}x + \int_0^T \int_\Omega D\frac{\partial C}{\partial x}\frac{\partial w}{\partial x}\,\mathrm{d}x\,\mathrm{d}t + \int_0^T \int_\Omega \left[\frac{\partial}{\partial x}\left(vCw - D\frac{\partial C}{\partial x}w\right)\right] \mathrm{d}x\,\mathrm{d}t$$
$$= \int_0^T \int_\Omega \left[M(C)\frac{\partial w}{\partial t} + vC\frac{\partial w}{\partial x}\right] \mathrm{d}x\,\mathrm{d}t + \int_0^T \int_\Omega fw\,\mathrm{d}x\,\mathrm{d}t \tag{7}$$

Next the temporal domain $[0,T]$ is divided into intervals $[t^n, t^{n+1}]$. The test function w is required to disappear for $t \notin [t^n, t^{n+1}]$ and to satisfy the formal adjoint equation

$$M(C)\frac{\partial w}{\partial t} + vC\frac{\partial w}{\partial x} = 0 \tag{8}$$

over $[t^n, t^{n+1}]$. While other choices of w are possible [33], eqn (8) corresponds to the standard approach [31]. It is important to note that eqn (8) is nonlinear in the concentration C but is linear in the test function w. Assuming that the concentration is continuous over the interval $[t^n, t^{n+1}]$ and applying Green's formula, we then have

$$\int_\Omega M[C(x,t^{n+1})]w(x,t^{n+1})\,\mathrm{d}x + \int_{t^n}^{t^{n+1}}\int_\Omega D\frac{\partial C}{\partial x}\frac{\partial w}{\partial x}\,\mathrm{d}x\,\mathrm{d}t$$
$$+ \int_{t^n}^{t^{n+1}}\int_{\partial\Omega}\left(vCw - D\frac{\partial C}{\partial x}w\right)\cdot n\,\mathrm{d}s\,\mathrm{d}t = \int_\Omega M[C(x,t^n)]w(x,t^n)\,\mathrm{d}x$$
$$+ \int_{t^n}^{t^{n+1}}\int_\Omega fw\,\mathrm{d}x\,\mathrm{d}t \tag{9}$$

Eqn (9) consists of five integrals corresponding to the total mass at the new time level, dispersion, boundary fluxes, mass at the old time level, and contributions from sources and sinks. There are several appealing features of this weak formulation. Specifically, it is in a fully conservative form and does not involve differentiating the isotherm $\omega_e(C)$, which is not Lipschitz continuous at the origin for a Freundlich isotherm with $0 < n_f < 1$ [4]; the range of non-Lipschitz continuity occurs routinely in applications [2].

Global mass conservation for our ELLAM approach can be seen by summing eqn (9) over all test functions $\{w_i\}$. If the test functions $\{w_i\}$ are required to satisfy $\sum_i w_i(x,t) = 1$, we obtain a statement of mass conservation for the domain Ω and the time interval $[t^n, t^{n+1}]$:

$$\int_\Omega M[C(x,t^{n+1})]\,\mathrm{d}x + \int_{t^n}^{t^{n+1}}\int_{\partial\Omega}\left(vC - D\frac{\partial C}{\partial x}\right)\cdot n\,\mathrm{d}s\,\mathrm{d}t =$$
$$\int_\Omega M[C(x,t^n)]\,\mathrm{d}x + \int_{t^n}^{t^{n+1}}\int_\Omega f\,\mathrm{d}x\,\mathrm{d}t \tag{10}$$

Before introducing the discrete approximation to eqn (9), we identify the characteristics associated with the original transport equation and adjoint equation, since these play an important role in the ELLAM approximation. The hyperbolic portion of eqn (1) has the characteristic speed

$$\lambda = \frac{v}{R_f} \tag{11}$$

$$R_f = 1 + \frac{d\varphi}{dC} \tag{12}$$

where R_f is the retardation factor [20]. The characteristics are the solution to

$$\frac{dx}{dt} = \lambda[C(x,t), x, t] = \lambda(C) = \frac{v}{1 + \frac{d\varphi}{dC}} \tag{13}$$

The characteristics for the adjoint eqn (8) are given instead by

$$\frac{dx}{dt} = \lambda_a[C(x,t), x, t] = \lambda_a[C(x,t)] \tag{14}$$

where the speed is

$$\lambda_a = \frac{vC}{C + \varphi(C)} \tag{15}$$

In general, both λ and λ_a are nonlinear functions of the concentration C. For the Freundlich isotherm from eqn (3) we have

$$\lambda = \frac{v}{1 + \frac{n_f K_f \rho_b}{\theta} C^{n_f - 1}}, \qquad \text{and}$$
$$\lambda_a = \frac{v}{1 + \frac{K_f \rho_b}{\theta} C^{n_f - 1}} \tag{16}$$

When $0 < n_f < 1.0$, which is the case we will focus on in our numerical experiments, $\frac{d\varphi}{dC} \to \infty$ as $C \searrow 0$ and both λ and $\lambda_a \to 0$. In addition, $|\lambda_a| < |\lambda| < |v|$ for $0 < n_f < 1.0$, since $K_f > 0$ by definition.

To provide a simple, concrete illustration of the solution and adjoint characteristic behavior around a front, we consider a Riemann problem with left and right concentrations $C_L = 0.9$ and $C_R = 0.1$. Figures 1 and 2 show λ and λ_a for $v = 1$, $D = 0.0$, and $\varphi(C) = 0.50085 \times C^{0.7}$. The solution is a right-going shock moving with Rankine-Hugoniot speed $\sigma = v(C_R - C_L)/[M(C_R) - M(C_L)]$. The

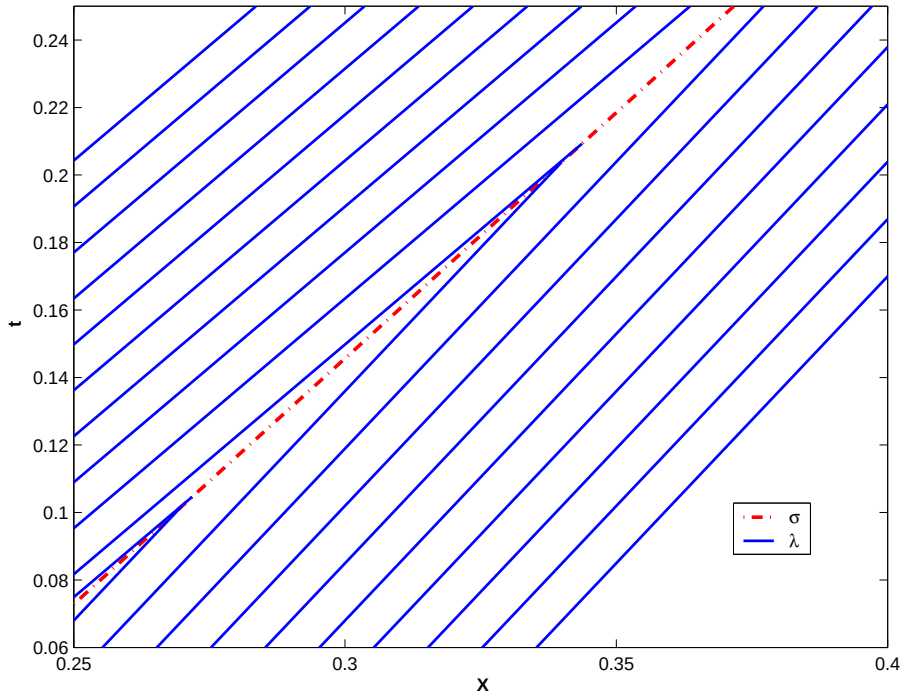

Fig. 1. λ Riemann example

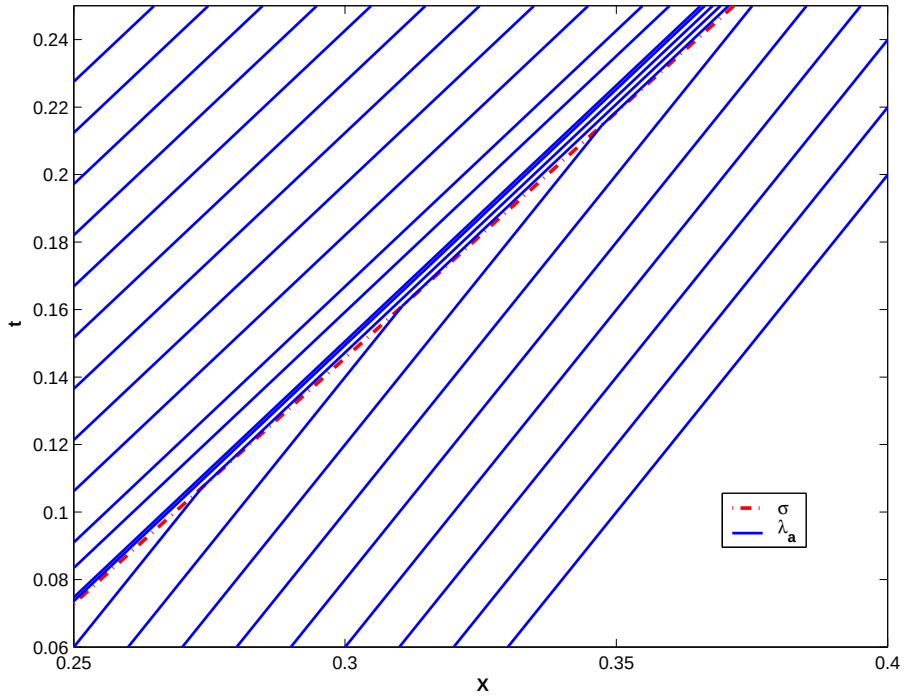

Fig. 2. λ_a Riemann example

characteristics defined by eqn (11) are straight lines in space-time at which a constant concentration value propagates. These intersect to form the shock

seen in Figure 1. On the other hand, the adjoint characteristics propagate constant values of the test function w, and are not straight since they depend on the solution C. At the shock, the adjoint characteristic speed jumps along with the solution value. The characteristic trajectory itself remains continuous, and the characteristics do not intersect. In the presence of physical dispersion, the solution characteristics may become close, but they will not cross. Similarly, the adjoint characteristic speeds will continue to change rapidly around a sharp front but will not undergo a jump in speed at the front.

3 Solution Approach

Our first step in developing a discrete approximation for the weak formulation, is to introduce a temporal approximation for the dispersion and source terms in eqn (9). Although second-order Runge-Kutta methods have been used in some cases [1], the most common approach is to use a backward Euler discretization in time so that the source and dispersion integrals only involve values at t^{n+1} [31]. With the backward Euler approximation, we have the semi-discrete system

$$\begin{aligned}
&\int_\Omega M[C(x,t^{n+1})]w(x,t^{n+1})\,\mathrm{d}x + \Delta t^{n+1}\int_\Omega D\frac{\partial C}{\partial x}(x,t^{n+1})\frac{\partial w}{\partial x}(x,t^{n+1})\,\mathrm{d}x \\
&+\int_{t^n}^{t^{n+1}}\int_{\partial\Omega}\left(vCw - D\frac{\partial C}{\partial x}w\right)\cdot n\,\mathrm{d}s\,\mathrm{d}t = \int_\Omega M[C(x,t^n)]w(x,t^n)\,\mathrm{d}x \\
&+\Delta t^{n+1}\int_\Omega f(x,t^{n+1})w(x,t^{n+1})\,\mathrm{d}x
\end{aligned} \tag{17}$$

where $\Delta t^{n+1} = t^{n+1} - t^n$.

We next must decide on a representation for the approximate solution to

C and the test function w. Our approach is essentially the same whether a FV-ELLAM or FE-ELLAM method is used. In the following, we detail both approaches and note differences that exist.

Since the problems considered here are one-dimensional, the spatial domain is simply $\Omega = [x_L, x_R]$. We introduce a discrete mesh $\mathcal{M}^h$ for Ω consisting of nodes or vertices $x_i, i = 0, \ldots, n_e$. $\mathcal{M}^h$ is a natural description of the computational mesh for an FE-ELLAM discretization, while we interpret $\mathcal{M}^h$ as a point-distributed grid with control volumes or cells around each of the interior vertices x_i, $i = 1, \ldots, n_e - 1$, so that $\Omega_i = [x_{i-1/2}, x_{i+1/2}]$, $x_{i+1/2} = (x_i + x_{i+1})/2$, and $|\Omega_i| = \Delta x_i = x_{i+1/2} - x_{i-1/2}$. In the following, we use the terms mesh and grid interchangeably to refer to $\mathcal{M}^h$ for convenience.

For both the FE-ELLAM and FV-ELLAM, the trial solution is represented using the standard linear Lagrangian basis functions

$$C(x,t) \approx \hat{C}(x,t) = \sum_{i=0}^{n_e} C_i(t)\psi_i(x) \tag{18}$$

where $\hat{C}(x,t)$ is the trial solution and $\psi_i(x)$ is supported on $[x_{i-1}, x_{i+1}]$

$$\psi_i(x) = \begin{cases} \frac{x - x_{i-1}}{\Delta x_{i-1/2}}, & x \in [x_{i-1}, x_i] \\ \frac{x_{i+1} - x}{\Delta x_{i+1/2}}, & x \in [x_i, x_{i+1}] \end{cases} \tag{19}$$

and $\Delta x_{i+1/2} = x_{i+1} - x_i$. The boundary trial functions are

$$\begin{aligned} \psi_0 &= \frac{x_1 - x}{\Delta x_{1/2}}, \quad x \in [x_L, x_1] \\ \psi_{n_e} &= \frac{x - x_{n_e-1}}{\Delta x_{n_e-1/2}}, \quad x \in [x_{n_e-1}, x_R] \end{aligned} \tag{20}$$

where $\Omega_0 = [x_0, x_{1/2}]$ and $\Omega_{n_e} = [x_{n_e-1/2}, x_{n_e}]$ at the boundaries for FV-ELLAM. In the following, we write $C(x,t)$ for the trial solution for conve-

nience.

At time level t^{n+1}, the test function w_i is aligned in a regular way with $\mathcal{M}^h$. Since w_i must obey eqn (8), this will not be the case in general for $t < t^{n+1}$. To reinforce this observation, we use the notation w_i^{n+1}:

$$w_i^{n+1}(x, t^{n+1}) = \quad \psi_i, \text{ for } i = 0, \ldots, n_e \qquad \text{FE-ELLAM} \tag{21}$$

$$w_i^{n+1}(x, t^{n+1}) = \begin{cases} 1, & x \in [x_{i-1/2}, x_{i+1/2}] \\ 0, & \text{otherwise} \end{cases} \qquad \text{FV-ELLAM} \tag{22}$$

Similarly, the FV-ELLAM boundary test functions w_0^{n+1} and $w_{n_e}^{n+1}$ are indicator functions associated with Ω_0 and Ω_{n_e}, respectively.

3.1 Evaluation of integrals

Given a choice of trial and test functions, the next step is to approximate the various integrals in eqn (17). Since we use a backward Euler approximation for the dispersion and source integrals (second and last terms in eqn (17)), these terms can be evaluated identically to similar terms that appear in standard ELLAM formulations for linear transport problems [8, 17].

3.1.1 mass at the new time level

The first term in eqn (17) accounts for the mass in Ω at the new time level. For FE-ELLAM we have the standard (nonlinear) mass integral for a Galerkin finite element method

$$\int_\Omega M(C^{n+1}) w_i^{n+1} \, \mathrm{d}x \text{ for } i = 0, \ldots, n_e \tag{23}$$

Similarly, for FV-ELLAM we have

$$\int_{\Omega} M(C(x,t^{n+1}))w_i^{n+1}(x,t^{n+1})\,\mathrm{d}x = \int_{\Omega_i} M(C(x,t^{n+1}))\,\mathrm{d}x \tag{24}$$

Eqns (23) and (24) can be approximated numerically in a straightforward manner. The usual approach for FV-ELLAM discretizations is to use a composite trapezoidal rule, which is exact for a linear problem [17]. A similar approach can be used here for both the FV-ELLAM and FE-ELLAM discretizations, although a larger number of subintervals may be required to approximate the nonlinear mass term accurately. Regardless of the quadrature used, it is also important for mass conservation that the numerical integration strategies chosen for the old and new mass integrals be consistent [17].

3.1.2 mass from the previous time level

Tracking along characteristics plays a major role in the remaining integrals, which account for boundary contributions and the mass in Ω at the previous time level. As a result, it is here that a nonlinear sorption isotherm can introduce significant complexity over conservative transport problems.

Following [15], we adopt the notation

$$x_a^*(t) = X_a(t;x,t^{n+1}) \equiv x - \int_t^{t^{n+1}} \lambda_a\{C[x_a^*(\tau),\tau], x_a^*(\tau),\tau\}\,\mathrm{d}\tau \tag{25}$$

$$\tilde{x}_a(t) = X_a(t;x,t^{n}) \equiv x + \int_{t^n}^{t} \lambda_a\{C[\tilde{x}_a(\tau),\tau], \tilde{x}_a(\tau),\tau\}\,\mathrm{d}\tau \tag{26}$$

for tracking along adjoint characteristics given by eqn (15). For tracking along solution characteristics we write

$$x^*(t) = X(t;x,t^{n+1}) \equiv x - \int_t^{t^{n+1}} \lambda\{C[x^*(\tau),\tau], x^*(\tau),\tau\}\,\mathrm{d}\tau \tag{27}$$

$$\tilde{x}(t) = X(t; x, t^n) \equiv x + \int_{t^n}^{t} \lambda\{C[\tilde{x}(\tau), \tau], \tilde{x}(\tau), \tau\} \, \mathrm{d}\tau \tag{28}$$

Approximating the first term on the right hand side of eqn (17) numerically gives

$$\int_{\Omega} M[C(x, t^n)] w_i^{n+1}(x, t^n) \, \mathrm{d}x \approx \sum_{q=0}^{n_q - 1} M[C^n(x_q)] w_i^{n+1}(x_q, t^n) r_q \tag{29}$$

where we define the set of integration points and weights $\{(x_q, r_q)\}$, $q = 0, \ldots, n_q - 1$ in physical space on Ω rather than on a reference element. n_q is the total number of integration points. We employ a forward-tracking approach where the integration weights and points are defined at t^n to ensure accurate evaluation of the mass at the old time level. The mass associated with each point is determined by evaluating $M[C^n(x_q)]$ at the interpolated concentration values, $C^n(x_q)$. Each integration point x_q is tracked forward to t^{n+1} by

$$\tilde{x}_q = (\tilde{x}_q)_a(t^{n+1}) = X_a(t^{n+1}; x_q, t^n) \tag{30}$$

using eqn (26). At t^{n+1}, the value of $w_i^{n+1}(\tilde{x}_q, t^{n+1})$ is determined using eqn (21) or eqn (22) depending upon the method used.

At a high level, approximating the mass term at t^n simply requires iterating through the list of integration points x_q at t^n and tracking them forward in time to t^{n+1} along characteristics defined by eqn (26). The right hand side vector components of eqn (17) for test functions w_i^{n+1} that are nonzero at $\tilde{x}_q$ then receive a corresponding contribution of mass. Unfortunately, accurately tracking the characteristics can be difficult even in one spatial dimension. As a result, a number of strategies have been developed to improve the tracking procedure's robustness. In particular, FV-ELLAM methods introduce an ap-

proximate test function W_i^{n+1} rather than use the actual value of w_i^{n+1} in eqn (29). W_i^{n+1} is roughly a smoothed out version of w_i^{n+1} with wider support covering three cells in one spatial dimension and is intended to help avoid some of the difficulties that arise in distributing mass at the new time level when tracking is inexact. The amount of smoothing for W_i^{n+1} is given in terms of the parameter NS [17]. For example, in the interior W_i^{n+1} can be written

$$W_i(x,t^{n+1}) = \begin{cases} 0, & x < x_{i-1/2} - \overline{\Delta x}_{i-1} \\ \frac{\Delta x_i}{\Delta x_{i-1}+\Delta x_i}\left(1 - \frac{x_{i-1/2}-x}{\overline{\Delta x}_{i-1}}\right), & x_{i-1/2} - \overline{\Delta x}_{i-1} \le x \le x_{i-1/2} \\ \frac{\Delta x_i + (x - x_{i-1/2})\Delta x_{i-1}/\overline{\Delta x}_i}{\Delta x_{i-1}+\Delta x_i}, & x_{i-1/2} \le x \le x_{i-1/2} + \overline{\Delta x}_i \\ 1, & x_{i-1/2} + \overline{\Delta x}_i \le x \le x_{i+1/2} - \overline{\Delta x}_i \\ \frac{\Delta x_i + (x_{i+1/2} - x)\Delta x_{i+1}/\overline{\Delta x}_i}{\Delta x_{i+1}+\Delta x_i}, & x_{i+1/2} - \overline{\Delta x}_i \le x \le x_{i+1/2} \\ \frac{\Delta x_i}{\Delta x_{i+1}+\Delta x_i}\left(1 - \frac{x - x_{i+1/2}}{\overline{\Delta x}_{i+1}}\right), & x_{i+1/2} \le x \le x_{i+1/2} + \overline{\Delta x}_{i+1} \\ 0, & x_{i+1/2} + \overline{\Delta x}_{i+1} \le x \end{cases} \tag{31}$$

where $\overline{\Delta x} = \Delta x/\mathrm{NS}$. FE-ELLAM continues to use $w_i^{n+1} = \psi_i$. Note that for $\mathrm{NS} = 2$, W_i^{n+1} is also piecewise-linear chapeau function. However, the FV-ELLAM and FE-ELLAM discretizations differ in their approximation of the new mass integral, since FV-ELLAM continues to use eqn (24) with w_i^{n+1} given by eqn (22).

We use the composite trapezoidal rule to approximate the mass integrals, because it has superior stability properties for Eulerian-Lagrangian discretizations [29] and allows the ability to adjust the number of subintervals per mesh cell based on the difficulty of a given problem [17]. We also follow the common practice for FV-ELLAM of introducing additional integration points known as

strategic spatial integration points (SSIPs) and strategic temporal integration points (STIPs). These SSIPs and STIPs are obtained by backtracking to t^n points where the approximate test functions W_i^{n+1} change slope and so improve the distribution of mass at the new time level. Defining the support of W_i^{n+1} in terms of NS and including SSIPs and STIPs has proven successful for a wide range of applications of FV-ELLAM [17, 31]. Usually, the number of intervals in the composite trapezoidal rule is also determined by NS. Since the problems here are nonlinear, we choose the number of subintervals per mesh cell in the composite trapezoidal rule based on accuracy requirements for the nonlinear mass term and use the NS parameter only to define the support of W_i^{n+1}.

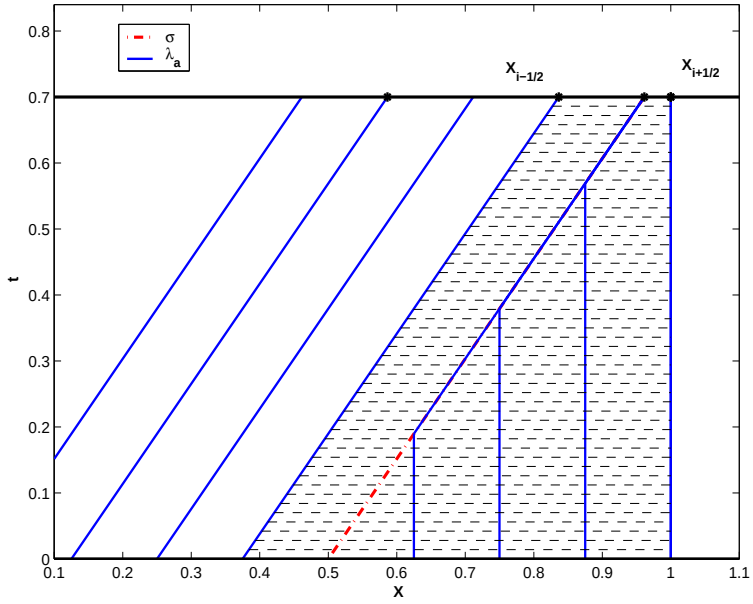

Fig. 3. Ω_i^* (shaded) Riemann example with $C_R = 0$

In the following, we address the approximation of boundary conditions and detail tracking procedures for the integration points $\{x_q\}$. Before turning to these topics, however, the behavior of solution and adjoint characteristics for zero concentration values bears some additional comment. For $0 < n_f < 1$,

the value $C = 0$ propagates with speed 0 even with non-zero dispersion [36]. If we consider the example Riemann problem from §2 with $C_R = 0$, we see that $\lambda_a = \sigma$. Adjoint characteristics moving with speed 0 intersect the shock and then move together at the shock speed (see Figure 3). If the shock intersects time level t^{n+1} at x_s^{n+1}, then $X_a(t^n; x_s^{n+1}, t^{n+1})$ is non-unique. Our ELLAM approach remains well-defined computationally and mathematically, however. In a FV-ELLAM context, for instance, if $x_s^{n+1} \in \Omega_i$ we can still determine the support of w_i^{n+1}

$$\Omega_i^* = [(x_{i-1/2})_a^*, (x_{i+1/2})_a^*] \tag{32}$$

from the points $(x_{i\pm1/2})_a^* = X_a(t^n; x_{i\pm1/2}^{n+1}, t^{n+1})$. If, say $x_s^{n+1} = x_{i+1/2}$, we choose to set $(x_{i+1/2})_a^* = x_{i+1/2}$, the right-most of the non-unique values. Moreover, since $M[C(x_q, t^n)] = 0$ for points x_q at t^n that map to x_s^{n+1}, the integral in eqn (29) is independent of this non-unique choice. Whenever the characteristics ahead of the shock carry nonzero mass ($C_R > 0$), as in Figure 2, they do not intersect, and $X_a(t^n; x_s^{n+1}, t^{n+1})$ is unique.

3.1.3 boundary integrals

The third integral in eqn (17) accounts for the influence of the physical boundary. Along the inflow boundary, eqn (17) contains an additional term, which for $\Gamma_I = x_L$ is

$$-\int_{t^n}^{t^{n+1}} q^b(x_L, t) w(x_L, t)\, \mathrm{d}t \tag{33}$$

Eqn (33) results in a contribution to the right hand side of eqn (17) for test functions w_i^{n+1} that intersect the inflow boundary over $[t^n, t^{n+1}]$. Eqn (33) can be approximated much as eqn (29) where the numerical quadrature is in time

along Γ_I [17]. Along the outflow boundary $\Gamma_O = x_R$ the zero-dispersive flux condition results in an additional term

$$\int_{t^n}^{t^{n+1}} v(x_R,t)C(x_R,t)w(x_R,t)\,\mathrm{d}t \tag{34}$$

that must be approximated. We simply use the trapezoidal rule

$$\int_{t^n}^{t^{n+1}} v(x_R,t)C(x_R,t)\,\mathrm{d}t \quad \approx \quad \frac{\Delta t^{n+1}}{2}\left[v(x_R,t^n)C_{n_e}^n + v(x_R,t^{n+1})C_{n_e}^{n+1}\right] \tag{35}$$

since this requires the solution from time levels t^{n+1} and t^n only [31]. However, sub time-stepping along Γ_O can be used for greater resolution if necessary.

3.2 Tracking techniques

In general, a numerical integration technique is required to solve eqn (14) and determine the behavior of the ELLAM test functions. There are many options for linear and nonlinear problems, including forward and backward Euler as well as explicit Runge-Kutta methods [10]. To track from point (x^0,τ^0) to $(\tilde{x}_a^1,\tau^1)$ with a backward Euler (BE) approximation, we set

$$\tilde{x}_a^1 = x^0 + \Delta\tau\lambda_a[C(\tilde{x}_a^1,\tau^1)] \tag{36}$$

while a simple second-order explicit Runge-Kutta (RK2) scheme is [10]

$$\begin{aligned}\tilde{x}_a^1 &= x^0 + \Delta\tau\lambda_a[C(x^0,\tau^0)]\\ \tau^1 &= \tau^0 + \Delta\tau\\ \tilde{x}_a^2 &= x^0 + \frac{\Delta\tau}{2}\left\{\lambda_a[C(x^0,\tau^0)] + \lambda_a[C(\tilde{x}_a^1,\tau^1)]\right\}\end{aligned} \tag{37}$$

where $\Delta\tau = \tau^1 - \tau^0$ is the tracking time step.

The ODE integration methods, eqns (36) and (37), are simple. For our purposes, the main challenge in applying them to solve eqn (14) is the evaluation of $\lambda_a[C(x,t)]$. Specifically, when integrating over the time interval $[t^n, t^{n+1}]$, the value of the approximate solution $C(x,t^n)$ and the nonlinear solver's current guess for $C(x,t^{n+1})$ will be known. However, determining $C(x,t)$ for $t \in (t^n, t^{n+1})$ requires interpolation based on a representation over $\Omega \times [t^n, t^{n+1}]$ for the approximate solution. There are a variety of approaches one could take to obtain such a representation with varying degrees of complexity depending on the assumptions made about the solutions behavior. If one wishes to use a tracking time step that is the same as the global time step, then eqn (37) or eqn (36) does not require interpolation at intermediate time levels. Of course, this suggests that the Courant number allowed may then be limited by the accuracy necessary for the tracking step. Below, we denote backward Euler time integration with $\Delta\tau = \Delta t^{n+1}$ as BE-S (backward Euler, single-step) and label the combination of RK2 time integration with $\Delta\tau = \Delta t^{n+1}$ as RK2-S (second order Runge-Kutta, single-step).

We also consider two approaches for obtaining intermediate values of C over $(t^n, t^{n+1}]$ to allow $\Delta\tau < \Delta t^{n+1}$. The first is to use bilinear interpolation (BL) in space and time based on $C(x,t^n)$ and the nonlinear solver's current guess for the solution at the new time level, $C^{n+1,m}(x,t^{n+1})$. The second approach is to use a front-tracking algorithm to obtain solution estimates at intermediate time levels, $t^{n,k} = t^n + k\Delta\tau$. Specifically, we employ a front-tracking method (FT) based on Risebro and Tveito [30] and implemented in Langseth [26], which computes a piecewise-constant solution to the homogeneous, hyperbolic portion of eqn (5),

$$\frac{\partial M(C)}{\partial t} + \frac{\partial (Cv)}{\partial x} = 0 \tag{38}$$

We then use the solution to eqn (38) to evaluate $\lambda_a[C(x, t^{n,k})]$ in eqn (36) or eqn (37). The advantage of using a front-tracking strategy over other approximate solution methods is that it can accurately locate sharp fronts that cause jumps in adjoint characteristic speeds and is not subject to a Courant number limitation [26, 30]. We note that the front-tracking method itself can not be applied directly to the original nonlinear transport problem due to the second-order dispersion term, but would require a splitting approach [19, 21].

The initial data for the FT front tracking could in principle be based on either $C(x, t^n)$ or on $C^{n+1,m}(x, t^{n+1})$. Here, we use $C(x, t^n)$ and track forward to t^{n+1}. To evaluate $\lambda_a[C(x, t^{n+1})]$ we use the tracking solution rather than $C^{n+1,m}(x, t^{n+1})$ so that the tracking procedure is independent of the solution at the new time level. This simplifies the Jacobian calculation and nonlinear solve dramatically, but eliminates a feedback mechanism present in the tracking strategies that incorporate $C^{n+1,m}(x, t^{n+1})$. Clearly, the front-tracking strategy outlined is more involved than bilinear interpolation or relying on solution values at t^n and t^{n+1} alone, but it could potentially allow significantly larger Courant numbers and so fewer nonlinear solves and tracking steps. We denote the overall tracking procedure RK2-FT or RK2-BL when either the FT or BL intermediate solution representation is combined with RK2 time integration.

We mention briefly the incorporation of boundary data in the tracking procedures. In general, one can simply use the corresponding value from the trial solution or from a given intermediate solution representation when evaluating λ_a at boundary locations. For Dirichlet conditions, the concentration at the

inflow boundary, C^b, can be used when evaluating λ_a. This may also be a reasonable approximation for total flux inflow boundary conditions in some cases, such as advection-dominated problems where an inflow concentration and flow rate are used to specify q^b.

3.3 Nonlinear and linear solvers

The FV-ELLAM and FE-ELLAM approximations presented above result in a discrete nonlinear system at each time level, which we solve using Newton's method. This nonlinear solve can be difficult for given sets of physical parameters and auxiliary data. To improve robustness, we use an Armijo line search strategy [22]. The performance of Newton's method can also be improved dramatically if a good initial guess for the solution is available. A default approach for solution of transient partial differential equations with implicit time discretizations is to use the solution from the previous time step as the initial guess for the solution at the new time level. Obviously, the quality of this guess degrades as the size of the time step increases if there is significant transient behavior in the problem. To improve performance, we use a crude, predicted value based on linear advection only. For the one-dimensional problems here, the initial guess for $v > 0$ is,

$$C_i^{n+1,0} = C_j^n, \quad j = i - \lfloor \mathrm{Cr} \rfloor \tag{39}$$

where $\lfloor x \rfloor$ is the largest integer less than or equal to x and Cr is the target Courant number for the simulation and corresponds to the maximum characteristic speed, $\mathrm{Cr} = \max_{i=0,n_e} |\lambda(C_i^n)| \Delta t^{n+1} / \Delta x$. For locations that track backwards out of the domain ($j < 0$ in eqn (39)), we set $C_i^{n+1,0}$ to the cor-

responding boundary value. The intent of eqn (39) is to speed convergence of the Newton solve. Its impact is largest for the RK2-S and BE-S tracking strategies, since they incorporate values of $C^{n+1,m}$ in the tracking of numerical integration points. If there is a nonlinear solver failure, the time step is halved and the Newton solve is repeated using the solution from the last unsuccessful iteration as the initial guess.

Since the Freundlich isotherm is not differentiable at $C = 0$ when $0 < n_f < 1$, we evaluate $\varphi(C)$ and $d\varphi/dC$ using cubic splines. Whether or not a tracking strategy depends on $C(x, t^{n+1})$ has a significant impact on the complexity associated with calculating analytical Jacobians for the Newton solve. We use a numerical Jacobian in the results below for simplicity. The linear solve needed at each Newton iteration was accomplished using a banded lower-upper decomposition solver from LAPACK [3].

4 Results

We next present a series of numerical experiments to evaluate our ELLAM approach for transport problems with self-sharpening fronts. The first set of simulations examine the FV-ELLAM and FE-ELLAM discretizations' performance with the RK2-S and BE-S tracking strategies on coarse grids and the discretizations' mass conservation properties. We then investigate the methods' ability to resolve fronts accurately as solutions become more steep. Last, we consider the performance of different tracking strategies for a range of Cr.

The basic test problems were constant injection into a domain originally free of contaminant and transport of a contaminant slug. The simulations are la-

beled according to their problem (PA–PF), which ELLAM discretization was used (FV or FE), and a simulation number. In all cases, the porosity and velocity were $\theta = 0.4$, $v = 1$. The final simulation time was $t = 0.5$, and sorption was modeled by a Freundlich isotherm with $K_f = 0.126$ and $n_f = 0.7$. Zero dispersive flux was applied at the outflow boundary. For the injection test problems, the inflow boundary condition corresponded to a constant concentration of one. Otherwise, the inflow boundary value was zero. The numerical quadrature used was the composite trapezoidal rule with six subintervals. The nonlinear systems in all simulations were solved using Newton's method with a numerical Jacobian and an ℓ_2 relative residual convergence criterion. The maximum number of nonlinear iterations and line searches allowed was twenty, and the nonlinear solver tolerance was 10^{-10} unless stated otherwise.

4.1 Initial results

For the first set of experiments, we considered a constant injection example (Problem A) and transport of a slug initial condition (Problem B) given by

$$C(x, t^0) = \begin{cases} 0, & 0 \le x < 0.15 \\ (x - 0.15)/0.05, & 0.15 \le x < 0.2 \\ 1, & 0.2 \le x < 0.3 \\ 1 - (x - 0.3)/0.05, & 0.3 \le x < 0.35 \\ 0, & 0.35 \le x \le 1 \end{cases} \tag{40}$$

The dispersion coefficient for the simulations was $D = 10^{-3}$. The other relevant parameters are presented in Table 1, where Pe is the mesh Peclet number, and NT is the number of composite trapezoidal rule intervals in time along the

inflow boundary. We note that Cr is the target Courant number for a given simulation and functions as an upper bound, since the time step is halved if there is a nonlinear solver failure.

Table 1

Run parameters for initial results

Run	Tracking	Δx	Pe	Cr	Run	Tracking	Δx	Pe	Cr
PA.FV.1	BE-S	1/50	20	4.5	PA.FV.6	RK2-S†	1/100	10	4.5
PA.FE.1	BE-S	1/50	20	4.5	PA.FE.6	RK2-S†	1/100	10	4.5
PA.FV.2	BE-S	1/100	10	4.5	PB.FV.1	RK2-S	1/50	20	4.5
PA.FE.2	BE-S	1/100	10	4.5	PB.FE.1	RK2-S	1/50	20	4.5
PA.FV.3	RK2-S*	1/50	20	4.5	PB.FV.2	RK2-S	1/100	10	4.5
PA.FE.3	RK2-S*	1/50	20	4.5	PB.FE.2	RK2-S	1/100	10	4.5
PA.FV.4	RK2-S*	1/100	10	4.5	PB.FV.3	BE-S	1/50	20	4.5
PA.FE.4	RK2-S*	1/100	10	4.5	PB.FE.3	BE-S	1/50	20	4.5
PA.FV.5	RK2-S†	1/50	20	4.5	PB.FV.4	BE-S	1/100	10	4.5
PA.FE.5	RK2-S†	1/50	20	4.5	PB.FE.4	BE-S	1/100	10	4.5

NS = 2; Problem A: NT = 16; Problem B: NT = 4

$*$ BE-S tracking for inflow boundary

† RK2-S tracking using $\lambda_a(C^b)$ at inflow boundary

Figures 4–7 illustrate the performance of the FV-ELLAM and FE-ELLAM discretizations with BE-S tracking for Problem A and RK2-S tracking for Problem B. The corresponding L_1, L_2, and mass balance values are reported in Tables 2 and 3. The dense grid solutions were obtained with a mass conservative finite difference discretization on grids with $\Delta x = 1/20000$ and $\Delta x = 1/50000$, respectively. For these simulations, the accuracy of the FV-ELLAM and FE-ELLAM discretizations was good. The FE-ELLAM discretization had lower

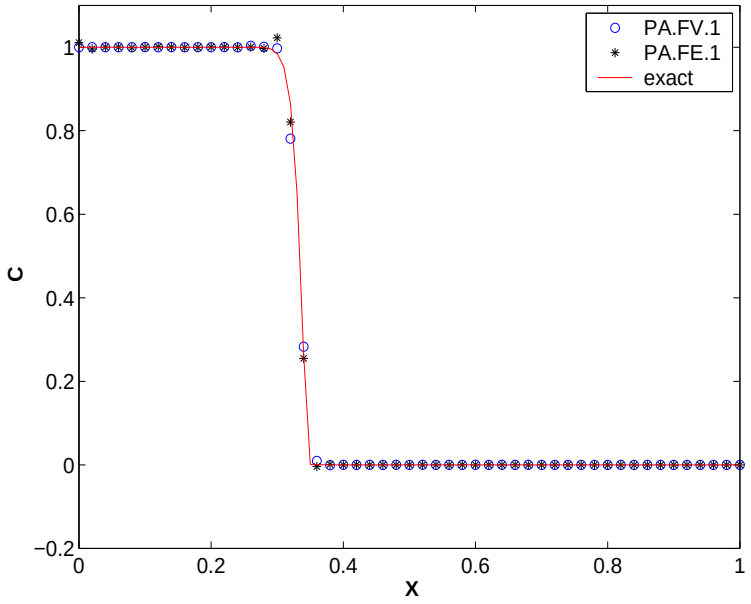

Fig. 4. ELLAM solutions Problem A, BE-S tracking, $\Delta x = 1/50$, $t = 0.5$

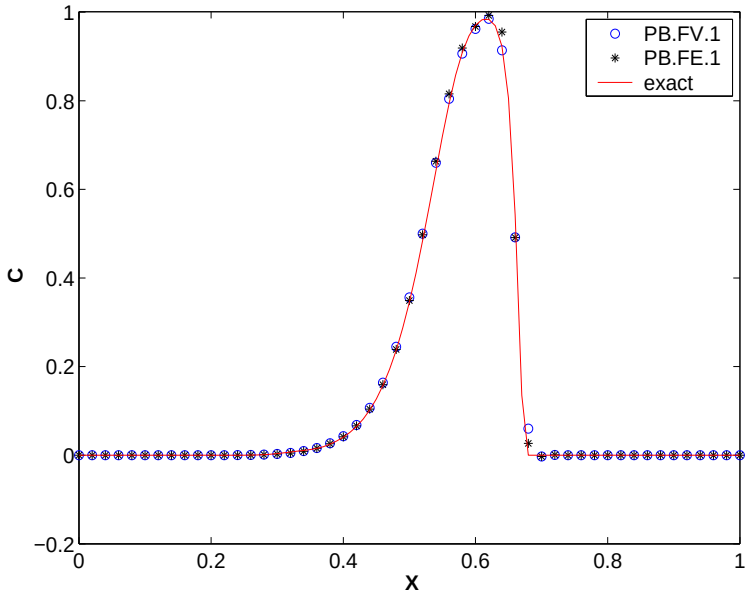

Fig. 5. ELLAM solutions Problem B, RK2-S tracking, $\Delta x = 1/50$, $t = 0.5$

L_1 and L_2 error, but had some overshoot for Run PA.FE.1. Otherwise, both spatial discretizations were able to represent the sharp fronts with negligible over or undershoot. The mass balance results were good for both methods with the FE-ELLAM mass error at the level of the nonlinear solver tolerance. The FV-ELLAM mass balance error was not as low as the FE-ELLAM error due

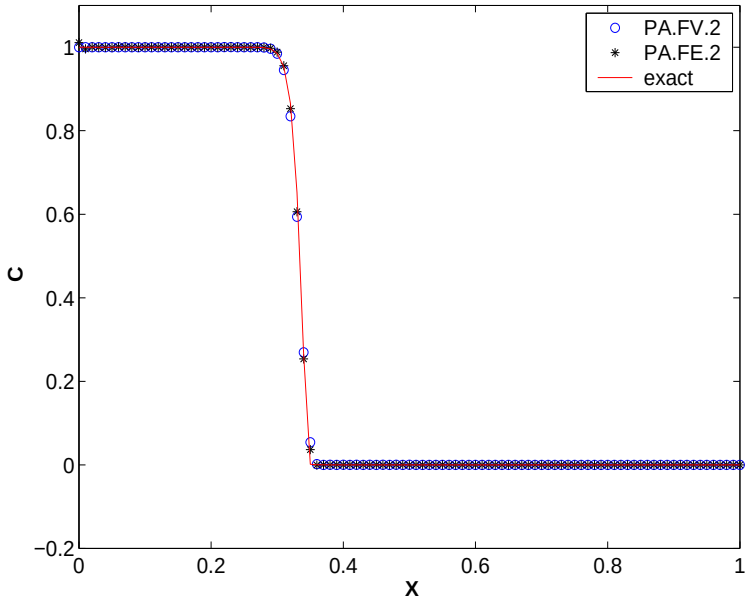

Fig. 6. ELLAM solutions Problem A, BE-S tracking, $\Delta x = 1/100$, $t = 0.5$

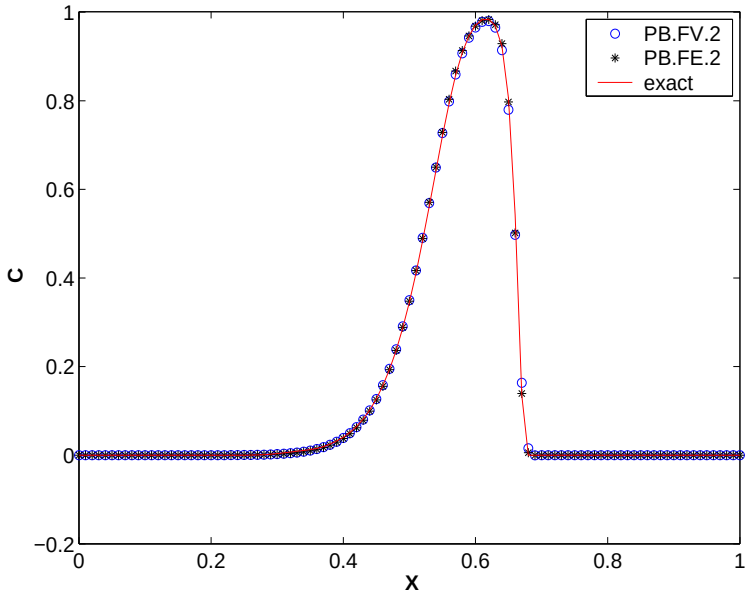

Fig. 7. ELLAM solutions Problem B, RK2-S tracking, $\Delta x = 1/100$, $t = 0.5$

to the use of SSIPs and STIPs. The strategic integration points increased the FV-ELLAM mass balance error to a level above the nonlinear solver residual because the numerical integration was not exact, and the collection of integration points changed from one time step to the next as a result of the addition of SSIPs and STIPs. Global mass conservation was still exact up to the non-

Table 2

ELLAM error results for Problem A

Run	L_1	L_2	rel. mass err
PA.FV.1	0.00514604	0.0225308	3.9826×10^{-6}
PA.FE.1	0.00444420	0.0186933	—
PA.FV.2	0.00225567	0.0110125	1.8040×10^{-6}
PA.FE.2	0.00177461	0.00862980	—
PA.FV.3	0.00440169	0.0201363	7.3856×10^{-6}
PA.FE.3	0.00413805	0.0171043	—
PA.FV.4	0.00165866	0.00839648	7.9678×10^{-6}
PA.FE.4	0.00130881	0.00651466	—
PA.FV.5	0.00442612	0.0202831	7.0136×10^{-6}
PA.FE.5	0.00414199	0.0171592	—
PA.FV.6	0.00167139	0.00842405	8.3992×10^{-6}
PA.FE.6	0.00130563	0.00650926	—

— less than 10^{-10}

linear solver tolerance for each step from t^n to t^{n+1}. However, the strategic integration points were defined by backtracking from the new time level locations where the approximate test functions W_i^{n+1} changed slope. For this reason, the total mass in the domain at the end of t^{n+1} defined by eqn (24) was in some cases slightly different than the sum in eqn (29) for the step from t^{n+1} to t^{n+2} due to the addition or subtraction of strategic integration points. This effect was small, however, and the overall solution quality was improved by the use of the STIP and SSIP points. We also note that the FV-ELLAM discretization achieved second-order convergence in space for Problem B for simulations where the time step was chosen small enough to eliminate tempo-

Table 3

ELLAM error results for Problem B

Run	L_1	L_2	rel. mass err
PB.FV.1	0.00665642	0.0208610	7.6067×10^{-5}
PB.FE.1	0.00520272	0.0172889	4.2842×10^{-10}
PB.FV.2	0.00284313	0.00917603	1.9665×10^{-5}
PB.FE.2	0.00228041	0.00713305	4.3568×10^{-10}
PB.FV.3	0.0126638	0.0287931	1.1267×10^{-4}
PB.FE.3	0.00735101	0.0197214	4.2842×10^{-10}
PB.FV.4	0.00485904	0.0130791	4.4658×10^{-5}
PB.FE.4	0.00336044	0.00983110	4.3568×10^{-10}

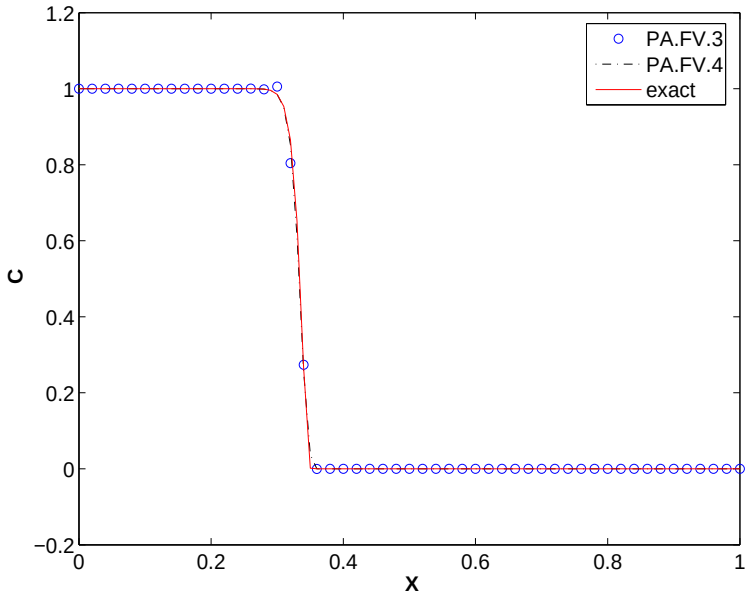

Fig. 8. FV-ELLAM solutions Problem A, RK2-S tracking with BE-S tracking at inflow, $\Delta x = 1/50, 1/100$, $t = 0.5$

ral truncation error [15].

In Runs PB.[FE,FV].3–4, we considered BE-S tracking for Problem B. The discretizations still resolved the fronts with negligible overshoot or undershoot

and produced good mass balance results, but the L_1 errors were 41% and 47% higher on the two spatial grids for FE-ELLAM using BE-S tracking. The FV-ELLAM L_1 errors with BE-S tracking were nearly twice as large as the RK2-S results. Moreover, the PB.FE.3 and PB.FE.4 simulations experienced one and two nonlinear solver failures, respectively, while the PB.FV.3 and PB.FV.4 runs had four and three nonlinear solver failures, respectively. Reducing the nonlinear solver tolerance to 10^{-7} and increasing the number of allowed iterations and line searches to 100 did not change the number of nonlinear solver failures or the simulations' basic behavior.

On the other hand, RK2-S tracking did not perform as well for Problem A because of the incompatibility between the initial data and the non-zero, total flux inflow boundary condition. The Newton solver experienced significant difficulties when C^n was used as the initial guess for the solution at C^{n+1}. Even with the initial guess from eqn (39), both FV-ELLAM and FE-ELLAM discretizations exhibited large overshoot at early times when the trial solution value was used to evaluate λ_a at the inflow boundary. There were at least two approaches to improve the RK2-S tracking performance. Given the advection-dominated nature of problem A, we considered incorporating a boundary concentration, $C^b = 1$, into the RK2-S tracking by using $\lambda_a(C^b)$ for points at the inflow boundary, x_L. Another solution was simply to use RK2-S tracking for interior points and BE-S tracking at the inflow boundary. The simulations with the combined tracking for Problem A are PA.[FE,FV].3–4. Simulations using $\lambda_a(C^b)$ for inflow boundary values are labeled PA.[FE,FV].5–6. The approaches performed similarly and eliminated the nonlinear solver difficulties. As the results in Table 2 and Figure 8 indicate, both strategies led to improved accuracy over BE-S tracking alone for the FE-ELLAM and FV-ELLAM spa-

tial discretizations.

4.2 Front resolution examples

In the runs for Problem A and Problem B, both the FV-ELLAM and FE-ELLAM discretizations were able to resolve the contaminant fronts adequately for a mesh width of $\Delta x = 1/50$, where the solution fronts spanned approximately three intervals. Given the use of a continuous, piecewise-linear representation for the trial solution, this is essentially the minimum we could expect and agrees with previous results for ELLAM and MMOC discretizations of linear transport problems [33]. For conditions where sharper fronts arise, say with less physical dispersion or lower Freundlich exponents, one can expect that the ELLAM discretizations would require finer grids to resolve the solution monotonically.

To be more specific, we looked at the discretizations' performance as the front widths in our test problems decreased. A straightforward way to do this was to look at traveling wave solutions to eqns (5)–(6) with boundary data corresponding to Problem A. That is, we sought a solution $C(\eta)$ to eqns (5)–(6) over the real axis with boundary data $C(-\infty) = C^*$ and $C(\infty) = C_*$ where $\eta = x - \alpha t$ and α is the wave speed [37]. For equilibrium sorption with a Freundlich isotherm and $C_* = 0$, van Duijn and Knabner [38] provide a closed form expression for the traveling wave solution

$$C(\eta) = \begin{cases} C^* \left\{ 1 - \exp\left[(1 - n_f) \left(\dfrac{v - \alpha}{D} \right) \eta \right] \right\}^{\frac{1}{1-n_f}}, & \text{for } \eta \leq 0 \\ 0, & \text{otherwise} \end{cases} \tag{41}$$

where the wave speed is

$$\alpha = v\frac{C^* - C_*}{\varphi(C^*) - \varphi(C_*) + C^* - C_*} \tag{42}$$

The solution front width can be determined by inverting eqn (41) for η

$$\begin{aligned}\eta &= \frac{\ln\left(1-(C/C^*)^{1-n_f}\right)}{(1-n_f)\left(\frac{v-\alpha}{D}\right)}, \quad \text{for } 0 < C < C^* \\ &= D\frac{\ln\left(1-(C/C^*)^{1-n_f}\right)}{(1-n_f)(v-\alpha)}\end{aligned} \tag{43}$$

and calculating the distance from the point $C = 0$ to the point where $C = C^*(1-\epsilon)$, since the solution to the problem is non-increasing. The front is located at $\eta = 0$, so we set the front width to be $d_{1-\epsilon} = |\eta[C^*(1-\epsilon)]|$. The front width for a fixed ϵ, $d_{0.99}$ for example, scales linearly with the dispersion D, while the front scales with $\sqrt{D}$ at a fixed time for the solution to the corresponding linear advection-dispersion problem [33]. In particular, eqn (43) suggests that if our ELLAM approximation needs roughly three intervals to resolve a front without overshoot or undershoot, then the minimum discretization required will be given by

$$\Delta x_{min} \approx d_{0.99}/3 \tag{44}$$

Table 4 gives run parameters for ELLAM calculations with $D = 2.5 \times 10^{-4}$, $\Delta x = 1/100, 1/200$, and an initial condition given by eqn (41). Aside from D, the physical parameters were identical to those for Problem A. The front width was $d_{0.99} = 1.4498 \times 10^{-2}$, so that $d_{0.99}/3 = 4.8327 \times 10^{-3}$. Figure 9 shows the solutions for $\Delta x = 1/100$ and Figure 10 shows the results for $\Delta x = 1/200$. The corresponding error values are reported in Table 5.

For Problem C, we performed simulations with FV-ELLAM using two different values of NS. NS = 2 represents a conservative choice, since the approximate

Table 4

Run parameters for Problem C

Run	Tracking	Δx	D	Pe	Cr	NS
PC.FV.1	RK2-S*	1/100	2.5×10^{-4}	40	4.5	2
PC.FE.1	RK2-S*	1/100	2.5×10^{-4}	40	4.5	-
PC.FV.2	RK2-S*	1/200	2.5×10^{-4}	20	4.5	2
PC.FE.2	RK2-S*	1/200	2.5×10^{-4}	20	4.5	-
PC.FV.3	RK2-S*	1/100	2.5×10^{-4}	40	4.5	16
PC.FV.4	RK2-S*	1/200	2.5×10^{-4}	20	4.5	16

NT = 16

$*$ BE-S tracking for inflow boundary

Table 5

ELLAM error results for Problem C

Run	L_1	L_2	rel. mass err
PC.FV.1	0.00307715	0.0231885	3.9674×10^{-5}
PC.FE.1	0.00321725	0.0218095	1.5572×10^{-10}
PC.FV.2	0.000984260	0.00967998	9.0764×10^{-6}
PC.FE.2	0.000921269	0.00836204	1.7097×10^{-9}
PC.FV.3	0.00443214	0.0305197	1.7577×10^{-4}
PC.FV.4	0.000906421	0.00828032	2.5945×10^{-5}

test function W_i^{n+1} is a piecewise-linear chapeau function. The wider support for NS = 2 has the effect of spreading mass over a larger area in the approximation of the old mass integral, eqn (29). Choosing NS = 16 narrows the support for W_i^{n+1} significantly and leads to a less diffusive approximation. As Figure 9 shows, the difference in the solutions with NS = 2 and NS = 16 for $\Delta x = 1/100$ was dramatic. However, for the finer grid with $\Delta x \approx d_{0.99}/3$ both approximations resolved the solution front accurately without spurious

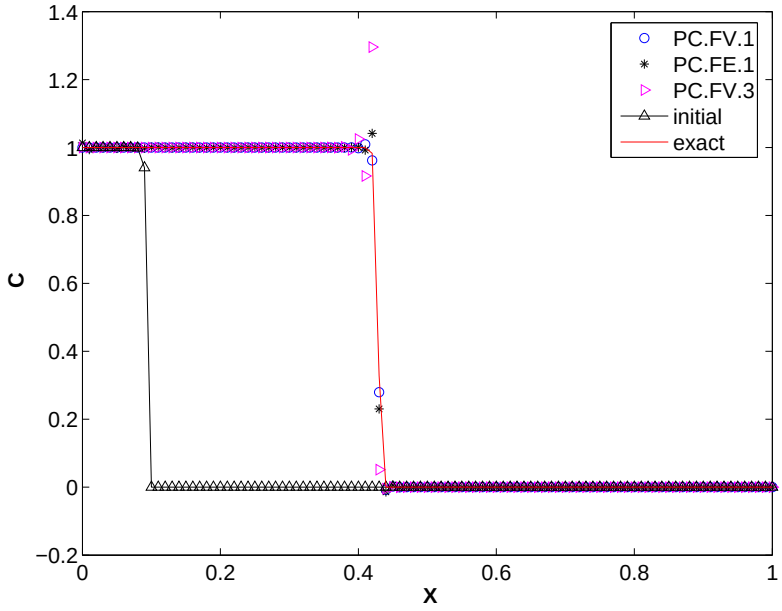

Fig. 9. ELLAM results for Problem C, $\Delta x = 1/100$, $t = 0.5$

oscillations.

The FV-ELLAM approximate test functions W_i^{n+1} are equivalent to FE-ELLAM test functions when NS=2. However, W_i^{n+1} is only used in the FV-ELLAM approximation of mass at t^n, so the discretizations are not identical. More precisely, the FE-ELLAM approximation to the mass at t^{n+1}, eqn (23), corresponds to a more distributed mass matrix than the FV-ELLAM approximation, eqn (24), and so contains less numerical diffusion [17, 25, 31]. As a result, the the FE-ELLAM approximation produced visible overshoot for the coarser grid but still resolved the front accurately for $\Delta x \approx d_{0.99}/3$.

We also performed simulations for the slug initial condition with $\Delta x = 1/100$, $1/200$, and $D = 2.5 \times 10^{-4}$. While not a traveling wave solution, the front behavior was similar to Problem C. Table 6 gives run parameters for Problem D and Table 7 gives the error values for the ELLAM calculations. Figures 11 and 12 show the results for the two grids. The dense grid solution was

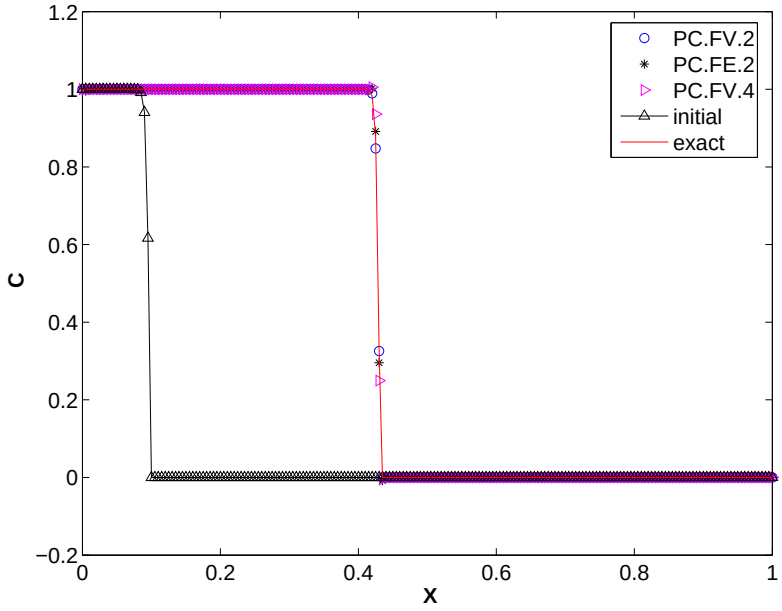

Fig. 10. ELLAM results for Problem C, $\Delta x = 1/200$, $t = 0.5$

again obtained with a mass conservative finite difference discretization on a grid with $\Delta x = 1/50000$. The relative performance of the discretizations was similar to Problem C. All the discretizations produced accurate solutions for $\Delta x \approx \Delta x_{min}$, but the FE-ELLAM and the FV-ELLAM discretization with NS = 16 exhibited overshoot on the $\Delta x = 1/100$ grid.

Table 6

Run parameters for Problem D

Run	Tracking	Δx	D	Pe	Cr	NS
PD.FV.1	RK2-S	1/100	2.5×10^{-4}	40	4.5	2
PD.FE.1	RK2-S	1/100	2.5×10^{-4}	40	4.5	-
PD.FV.2	RK2-S	1/200	2.5×10^{-4}	20	4.5	2
PD.FE.2	RK2-S	1/200	2.5×10^{-4}	20	4.5	-
PD.FV.3	RK2-S	1/100	2.5×10^{-4}	40	4.5	16
PD.FV.4	RK2-S	1/200	2.5×10^{-4}	20	4.5	16

NT = 4

Table 7

ELLAM error results for Problem D

Run	L_1	L_2	rel. mass err
PD.FV.1	0.00375488	0.0222302	2.9905×10^{-5}
PD.FE.1	0.00373496	0.0211762	-
PD.FV.2	0.00127395	0.00884059	1.6434×10^{-5}
PD.FE.2	0.00115919	0.00777404	8.7131×10^{-10}
PD.FV.3	0.00398739	0.0218459	9.6868×10^{-5}
PD.FV.4	0.00114844	0.00777340	3.5685×10^{-5}

- less than 10^{-10}

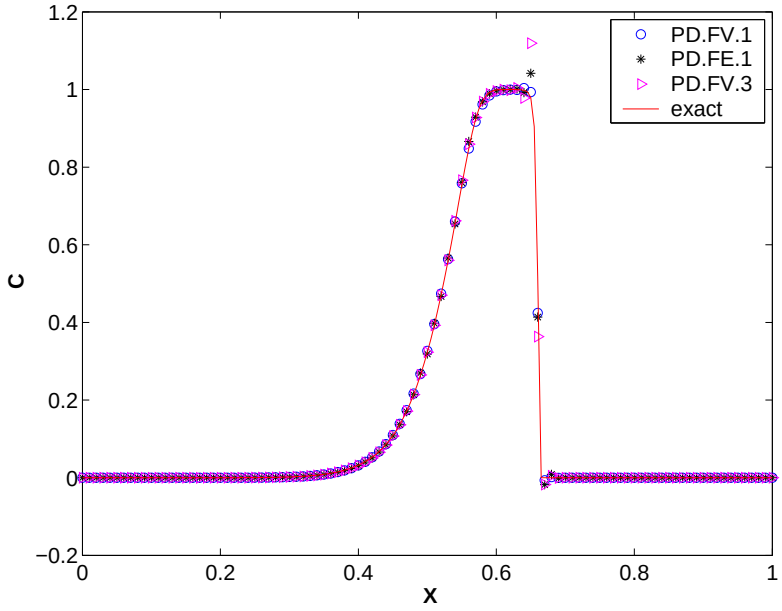

Fig. 11. ELLAM results for Problem D, $\Delta x = 1/100$, $t = 0.5$

4.3 Tracking comparison

The simulations for Problems A–D were performed using the RK2-S and BE-S tracking strategies, which required $\Delta\tau = \Delta t^{n+1}$. While we were able to obtain good results for Cr = 4.5, relying solely on characteristic speeds from t^n and

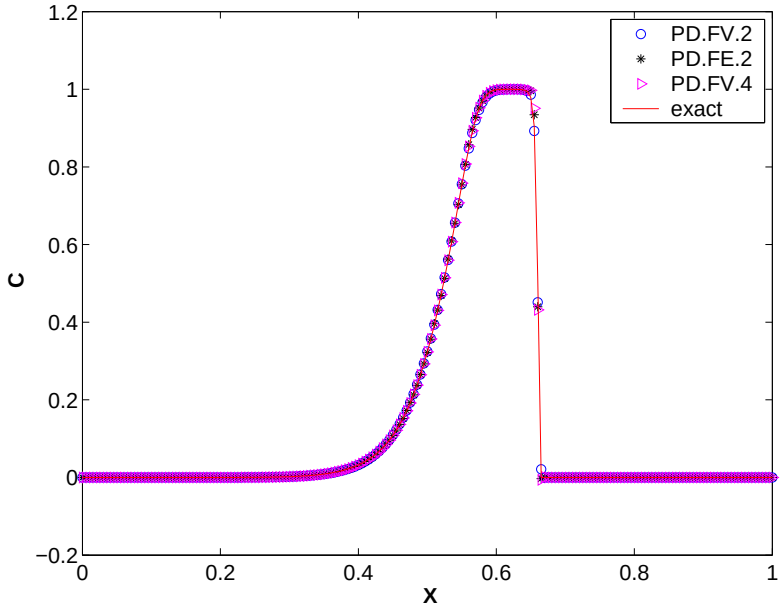

Fig. 12. ELLAM results for Problem D, $\Delta x = 1/200$, $t = 0.5$

t^{n+1} is less tenable as Cr increases significantly. We next compared the RK2-S tracking to the RK2-BL and RK2-FT strategies with $\Delta\tau = \Delta t^{n+1}/n_{st}$, where the number of tracking substeps, n_{st}, was greater than one. First, we compared the RK2-FT and RK2-BL strategies for moderate Cr where the RK2-S strategy performed well. The physical parameters for the first set of simulations (Problem E) were identical to Problem B. We then used the physical parameters and initial condition from Problem D to compare the tracking strategies for significantly larger Cr (Problem F).

Tables 8 and 9 contain the relevant parameters for the simulations of Problem E and Problem F, respectively. The main parameters controlling the performance of the RK2-FT method are the discretization parameter δ_{fr} and the wave speed cutoff, c_{fr}. δ_{fr} determines the number of fronts used to represent the solution initially and the number of shock waves used to approximate a rarefaction. c_{fr} is used along with δ_{fr} to provide a minimum wave strength required for a front to be incorporated in the solution approximation. Specifi-

cally, a front is tracked if the magnitude of the jump across the front is greater than $c_{fr}\delta_{fr}$ [26].

Table 8

Run parameters for Problems E

Run	Tracking	Δx	D	Pe	Cr	n_{st}	δ_{fr}	c_{fr}
PE.FV.1	RK2-BL	1/50	1.0×10^{-3}	20	4.5	2	-	-
PE.FE.1	RK2-BL	1/50	1.0×10^{-3}	20	4.5	2	-	-
PE.FV.2	RK2-FT	1/50	1.0×10^{-3}	20	4.5	2	1/50	0.01
PE.FE.2	RK2-FT	1/50	1.0×10^{-3}	20	4.5	2	1/50	0.01
PE.FV.3	RK2-BL	1/100	1.0×10^{-3}	10	4.5	2	-	-
PE.FE.3	RK2-BL	1/100	1.0×10^{-3}	10	4.5	2	-	-
PE.FV.4	RK2-FT	1/100	1.0×10^{-3}	10	4.5	2	1/100	0.01
PE.FE.4	RK2-FT	1/100	1.0×10^{-3}	10	4.5	2	1/100	0.01
PE.FV.5	RK2-FT	1/100	1.0×10^{-3}	10	4.5	2	1/50	0.01
PE.FE.5	RK2-FT	1/100	1.0×10^{-3}	10	4.5	2	1/50	0.01
PE.FV.6	RK2-FT	1/100	1.0×10^{-3}	10	4.5	2	1/200	0.01
PE.FE.6	RK2-FT	1/100	1.0×10^{-3}	10	4.5	2	1/200	0.01

NS = 2, NT = 4

Figure 13 shows FV-ELLAM solutions from the RK2-BL and RK2-FT tracking strategies for Problem E with $\Delta x = 1/50$ and Cr = 4.5. For comparison, the solution using RK2-S tracking, Run PB.FV.1, is included as well. Table 10 includes the L_1, L_2, and mass balance errors for the RK2-BL and RK2-FT tracking strategies. The results for the RK2-BL tracking were much poorer than either the RK2-S or the RK2-FT methods, producing large overshoot on both the $\Delta x = 1/50$ and $\Delta x = 1/100$ grids. The RK2-FT solutions were less accurate than the RK2-S results for the same Cr for both the FE-ELLAM

Table 9

Run parameters and results for Problems F

Run	Tracking	Δx	D	Pe	Cr	n_{st}	δ_{fr}	c_{fr}
PF.FE.1	RK2-FT	1/200	2.5×10^{-4}	20	16.5	2	1/200	0.01
PF.FV.1	RK2-FT	1/200	2.5×10^{-4}	20	16.5	2	1/200	0.01
PF.FE.2	RK2-S	1/200	2.5×10^{-4}	20	16.5	1	-	-
PF.FV.2	RK2-S	1/200	2.5×10^{-4}	20	16.5	1	-	-
PF.FE.3†	RK2-S	1/200	2.5×10^{-4}	20	16.5	1	-	-
PF.FV.3†	RK2-S	1/200	2.5×10^{-4}	20	16.5	1	-	-
PF.FE.4	RK2-FT	1/200	2.5×10^{-4}	20	16.5	2	1/100	0.01
PF.FV.4	RK2-FT	1/200	2.5×10^{-4}	20	16.5	2	1/100	0.01

NT = 4

† nonlinear solver tolerance 10^{-6}, max 100 line searches, 100 nonlinear iterations

and FV-ELLAM spatial discretizations. While fronts were similarly resolved, the L_1 error for the RK2-FT Runs was 35% higher for FV-ELLAM and 19% higher for FE-ELLAM on the $\Delta x = 1/50$ grid.

The impact of δ_{fr} on the accuracy of the RK2-FT tracking can be seen in Runs PE.[FV,FE].4–PE.[FV,FE].6. RK2-FT tracking with $\delta_{fr} = 1/100$ and $\delta_{fr} = 1/200$ produced L_1 and L_2 errors that were comparable to the errors from the corresponding RK2-S tracking solutions. Increasing δ_{fr} to $2\Delta x$ produced less accurate results, as can be seen in Figure 14 and Table 10.

Since the RK2-BL strategy performed poorly for Problem E, we considered only the RK2-S and RK2-FT approaches for the problem with less physical dispersion. Figure 15 shows the solutions from the RK2-S and RK2-FT strategies with FV-ELLAM and FE-ELLAM spatial discretizations for a tar-

Table 10

Run results for Problems E

Run	L_1	L_2	rel. mass err
PE.FV.1	0.0155545	0.0383824	4.1861×10^{-5}
PE.FE.1	0.0160688	0.0396553	-
PE.FV.2	0.00899326	0.0240897	6.6298×10^{-5}
PE.FE.2	0.00620536	0.0188605	-
PE.FV.3	0.00674198	0.0184749	2.4097×10^{-5}
PE.FE.3	0.00711775	0.0191097	4.3568×10^{-10}
PE.FV.4	0.00359544	0.0112651	2.7236×10^{-5}
PE.FE.4	0.00235988	0.00807344	8.7136×10^{-10}
PE.FV.5	0.00802655	0.0153431	3.1588×10^{-5}
PE.FE.5	0.00698441	0.0132661	4.3568×10^{-10}
PE.FV.6	0.00334196	0.0111522	1.7654×10^{-5}
PE.FE.6	0.00221380	0.00813326	-

- less than 10^{-10}

get Cr = 16.5, while Table 11 gives the L_1, L_2, and mass balance errors as well as the total number of time steps taken and nonlinear solver iterations for the simulations. The spatial discretizations performed similarly. Results with both tracking approaches captured the sharp front well with negligible mass balance error.

The L_1 and L_2 errors for the RK2-S and RK2-FT simulations with $\delta_{fr} = \Delta x$ were similar. The FE-ELLAM errors with RK2-S tracking were lower than those for FE-ELLAM with RK2-FT tracking, while the opposite was true for the FV-ELLAM discretization. The RK2-FT results with $\delta_{fr} = 2\Delta x$ were much poorer. Although the accuracy in Runs PF.[FE,FV].2 was comparable

Table 11

Run results for Problems F

Run	L_1	L_2	rel. mass err	time steps	nl its
PF.FV.1	0.00217702	0.0129708	3.2722×10^{-6}	5	27
PF.FE.1	0.00196901	0.0122595	1.3070×10^{-9}	5	28
PF.FV.2	0.00240612	0.0106530	1.6912×10^{-4}	54	462
PF.FE.2	0.00134290	0.00757244	1.7426×10^{-9}	46	425
PF.FV.3	0.00189700	0.0102873	1.9320×10^{-4}	36	362
PF.FE.3	0.00134111	0.00757331	6.8370×10^{-5}	53	433
PF.FV.4	0.00594223	0.0162554	9.1099×10^{-6}	5	27
PF.FE.4	0.00592168	0.0161490	-	5	30

- less than 10^{-10}

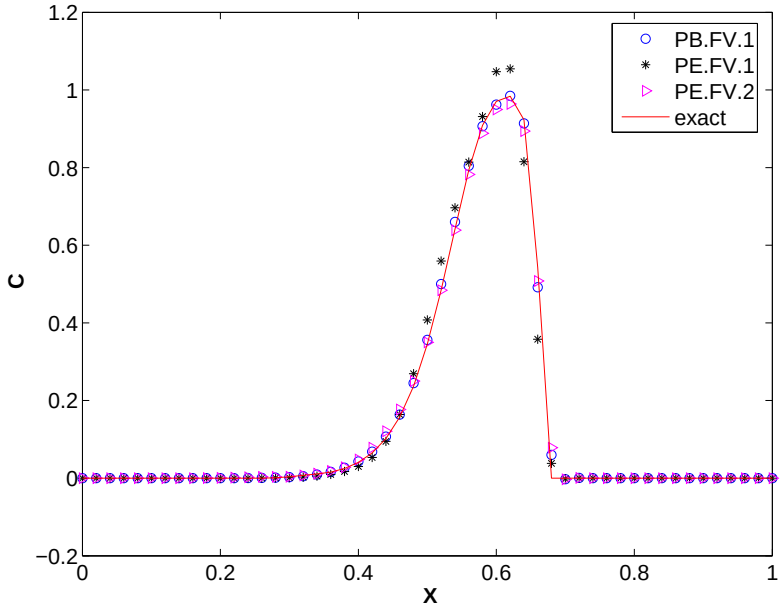

Fig. 13. FV-ELLAM results for Problem E, RK2-S, RK2-BL, and RK2-FT tracking, $\Delta x = 1/50$, $t = 0.5$

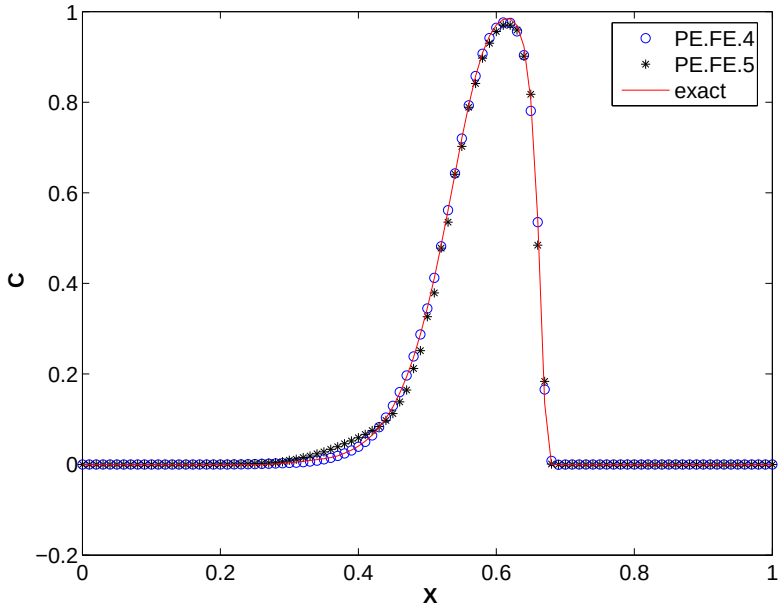

Fig. 14. FE-ELLAM results for Problem E, RK2-FT tracking $\delta_{fr} = 1/50, 1/100$, $\Delta x = 1/100$, $t = 0.5$

to that in Runs PF.[FE,FV].1, Cr = 16.5 was too large for the RK2-S tracking. Both Runs PF.FV.2 and PF.FE.2 experienced repeated nonlinear solver failures due to the larger target Cr. The FV-ELLAM simulation had 16 failures and took 54 time steps, while the FE-ELLAM calculation had 14 failures and 46 time steps overall. The total number of nonlinear iterations was an order of magnitude higher as well. The failure modes for the Newton solver consisted of both stagnation in the Armijo line search and exhausting the allowed nonlinear iterations. Since the relative residual tolerance of 10^{-10} was rather tight, Runs PF.FV.3 and PF.FE.3 were performed with a tolerance of 10^{-6} and a maximum of 100 nonlinear iterations and line searches. The reduced tolerance decreased the number of failures for FV-ELLAM to 13 but increased the number of failures for the FE-ELLAM simulation to 15. The number of time steps and nonlinear iterations required were still an order of magnitude higher for the RK2-S tracking simulations.

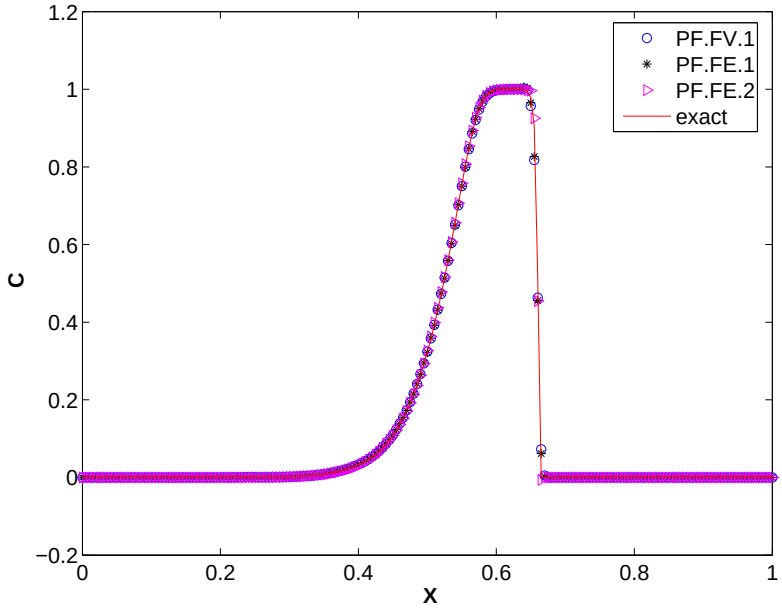

Fig. 15. ELLAM results for Problem F, RK2-S and RK2-FT tracking, $\Delta x = 1/200$, $t = 0.5$

5 Discussion

The test problems we considered were challenging because they involved self-sharpening fronts with small physical dispersion as well as rarefaction tails. While there were some differences, the performance and accuracy of the FV-ELLAM and FE-ELLAM discretizations were comparable in the numerical experiments. Both discretizations resolved the fronts accurately as long as the mesh width was sufficient to allow three elements on a front. FE-ELLAM generally produced lower L_1 and L_2 error but was more prone to overshoot or undershoot on coarse grids than FV-ELLAM with NS=2. With NS=2, our FV-ELLAM approach had more numerical diffusion than FE-ELLAM due to the differences in their approximations for the mass at t^{n+1} [17, 25, 31]. Higher values of NS reduced the numerical diffusion for FV-ELLAM and improved accuracy for sufficiently resolved calculations, but naturally increased

the likelihood of spurious oscillations on coarse grids. In general, there was the familiar tradeoff between accuracy in smooth regions and the ability to represent fronts monotonically [27]. Steeper physical solutions required finer discretizations or an approximation with greater numerical diffusion to create fronts with a minimum width for a given grid.

The global mass balance errors for the FE-ELLAM and FV-ELLAM discretizations were good. The FE-ELLAM mass balance error was at the nonlinear solver tolerance, while the FV-ELLAM errors were below 2×10^{-4} for all the simulations. The FV-ELLAM mass balance error was not as low as the FE-ELLAM error due to the use of SSIPs and STIPs [15]. On the other hand, the SSIPs and STIPs improved the overall performance of the FV-ELLAM discretization, and the FV-ELLAM relative mass balance errors remained small. The impact of the strategic integration points on global mass balance can be reduced by increasing the accuracy of the quadrature through, for instance, adding more intervals in the composite trapezoidal rule formulas.

We explored two time discretizations, BE and RK2, for tracking numerical integration points forward from t^n to t^{n+1}. The first-order BE method was not as accurate as the second-order RK2 approximation when using characteristic information from t^n and t^{n+1} alone. On the other hand, it was useful for tracking from the inflow boundary when $q^b > 0$. One of the advantages of ELLAM is that the tracked integration points are independent of one another, so it was then simple to combine different tracking procedures within the same simulation.

Since tracking required information about the solution to evaluate the adjoint characteristics, we also investigated different approaches for obtaining

a solution representation at times $t > t^n$. The RK2-S approach, which was simple and relied solely on C^n and $C^{n+1,m}$ worked well for Cr up to 4.5 in the numerical experiments when combined with the initial guess from eqn (39). In general, an upper bound on the time step for the RK2-S approach depends on the difficulty of the problem and the spatial discretization, including the amount of numerical diffusion. For time steps that were too large, poor performance of the RK2-S tracking algorithm manifested itself through nonlinear solver failures for the target time step, which in turn led to time step reductions in order to obtain convergence. On the other hand, the RK2-FT tracking strategy, which combined RK2 time integration and a front-tracking method to provide intermediate solution values, allowed the FE-ELLAM and FV-ELLAM methods to obtain good solutions for very large time steps.

Accuracy of the intermediate representation naturally affected the overall solution accuracy, since the tracking dictated the mass distribution from the previous time step. Using bilinear interpolation to obtain intermediate solution representations (RK2-BL) performed poorly. For smaller time steps where the RK2-S tracking succeeded, the RK2-FT solutions generally had higher L_1 and L_2 error values than those from the RK2-S tracking algorithm. Simulations with the two tracking strategies resolved fronts similarly. Rather, the increased error for the RK2-FT approximation was largely around rarefactions. Increasing δ_{fr} improved the FT algorithm's approximation of rarefactions and in turn reduced the solution error.

In our numerical experiments, both the FV-ELLAM and FE-ELLAM discretizations resolved the self-sharpening fronts monotonically as long as the mesh width was sufficient to allow three intervals on a front. This places an increasing computational burden on the discretizations as fronts in a prob-

lem steepen due, for example, to reduced physical dispersion. On the other hand, increased numerical diffusion can always be introduced using techniques such as mass lumping [31, 34] in order to widen solution fronts sufficiently to meet the requirements on a given mesh. Another alternative to improve performance is to employ adaptive refinement around the front using patch-based local refinement [39] or a moving mesh approach [43, 44] in order to provide the minimal resolution necessary around fronts with coarser discretizations in areas of smoother solution behavior.

We have not addressed the issue of computational efficiency in this work. For multidimensional nonlinear problems, we expect the expense and success of our approach to be dictated largely by the tracking procedure for numerical integration points. Here, we have identified promising strategies for one-dimensional problems. The RK2-S tracking is simple to implement and inexpensive on a per iteration basis. The RK2-FT is more involved since it requires the initialization and solution of a front-tracking problem every time step. However, the RK2-FT allowed much larger time steps than the RK2-S tracking for the problems considered. Another aspect of the RK2-FT tracking procedure, as implemented here, was that it was independent of the solution at the new time level. While this was not necessary, it did simplify the Jacobian calculation and behavior of the nonlinear systems dramatically, which could offer a significant advantage for multidimensional problems.

While our initial results are promising given the straightforward nature of the formulation, more work is required to evaluate its performance for systems which present significantly more complicated characteristic behavior and for multidimensional problems. For problems in two and three spatial dimensions, much of the current approach can be extended naturally following previous

ELLAM work [8, 18]. The main challenge will be to develop effective tracking procedures given the added nonlinearity of the adjoint characteristics.

6 Conclusions

In this work, we formulated FV-ELLAM and FE-ELLAM approximations for advective-dispersive transport with nonlinear equilibrium sorption. We performed a series of numerical experiments to evaluate the discretizations' front resolution, mass balance properties, and ability to take large time steps while maintaining accuracy. Based on our work, we draw the following conclusions:

- Our ELLAM formulation produces solutions that maintain the mass-conservation properties for which ELLAMs are known. Both FV-ELLAM and FE-ELLAM discretizations based on our approach can be expected to resolve self-sharpening fronts monotonically for one-dimensional reactive transport problems as long as the spatial discretization is sufficiently fine to allow three intervals on a front.
- The RK2-S tracking approach points provides a straightforward procedure for tracking numerical integration points that can perform well for Courant numbers several times larger than one.
- The RK2-FT tracking approach, while more involved than the RK2-S algorithm, allows our ELLAM approaches to take very large time steps and still produce accurate solutions.

Acknowledgments

The efforts of MWF and CTM were supported the National Science Foundation through DMS-0112069, and grant P42 ES05948 from the National Institute of Environmental Health Sciences. The research of TFR was supported in part by NSF Grants DMS-0084438 and DMS-0222300. CEK was supported in part by ARO grant DAAD19-02-1-0391.

References

[1] M. Al-Lawatia, R.C. Sharpley, and H. Wang. Second-order characteristic methods for advection-diffusion equations and comparison to other schemes. *Advances in Water Resources*, 22(7):741–768, 1999.

[2] R. M. Allen-King, P. Grathwohl, and W.P. Ball. New modeling paradigms for the sorption of hydrophobic organic chemicals to heterogeneous carbonaceous matter in soils, sediments, and rocks. *Advances in Water Resources*, 25(8–12):985–1016, 2002.

[3] E. Anderson, Z. Bai, C. Bischof, J. Demmel, J. Dongarra, J. Du Croz, A. Greenbaum, S. Hammarling, A. McKenney, S. Ostrouchov, and D. Sorensen. *LAPACK Users' Guide*. SIAM, Philadelphia, PA, 1992.

[4] J.W. Barrett and P. Knabner. An improved error bound for a Lagrange-Galerkin method for contaminant transport with non-Lipschitzian adsorption kinetics. *SIAM Journal on Numerical Analysis*, 35(5):1862–1882, 1998.

[5] D. A. Barry, H. Prommer, C. T. Miller, P. K. Engesgaard, A. Brun, and C. Zheng. Modelling the fate of oxidisable organic contaminants in groundwater. *Advances in Water Resources*, 25(8–12):945–983, 2002.

[6] L.S.J. Bell and P.J. Binning. A split operator approach to reactive transport with the forward particle tracking Eulerian-Lagrangian localized adjoint method. *Advances in Water Resources*, 27:323–334, 2004.

[7] P. Binning and M.A. Celia. A finite volume Eulerian-Lagrangian localized adjoint method for solution of contaminant transport equations in two-dimensional multiphase flow systems. *Water Resources Research*, 32(1): 103–147, 1996.

[8] P. Binning and M.A. Celia. A forward particle tracking Eulerian-Lagrangian Localized Adjoint Method for solution of the contaminant transport equation in three dimensions. *Advances in Water Resources*, 25:147–157, 2002.

[9] M.A. Celia, T. F. Russell, I. Herrera, and R.E. Ewing. An Eulerian-Lagrangian localized adjoint method for the advection-diffusion equation. *Advances in Water Resources*, 13:187–206, 1990.

[10] G. Coppola, S.J. Sherwin, and J. Peiró. Nonlinear particle tracking for high-order elements. *Journal of Computational Physics*, 172:356–386, 2001.

[11] H.K. Dahle, R.E. Ewing, and T.F. Russell. Eulerian-Lagrangian localized adjoint methods for a nonlinear advection-diffusion equation. *Computer Methods in Applied Mechanics and Engineering*, 122:223–250, 1995.

[12] C.N. Dawson, C.J. van Duijn, and M.F. Wheeler. Characteristic-Galerkin methods for contaminant transport with nonequilibrium adsorption kinetics. *SIAM Journal on Numerical Analysis*, 31:982–999, 1994.

[13] J. Douglas Jr and T.F. Russell. Numerical methods for convection-dominated diffusion problems based on combining the method of characteristics with finite element or finite difference procedures. *SIAM Journal on Numerical Analysis*, 19(5):871–885, 1982.

[14] R.E. Ewing and H. Wang. A summary of numerical methods for time-dependent advection-dominated partial differential equations. *Journal of Computational and Applied Mathematics*, 128:423–445, 2001.

[15] M.W. Farthing, C.E. Kees, T.F. Russell, and C. T. Miller. An ELLAM approximation for advective-dispersive transport with nonlinear sorption. In C.T. Miller, M.W. Farthing, W.G. Gray, and G.F. Pinder, editors, *Computational Methods in Water Resources XV*, volume 1, pages 505–518, Amsterdam, The Netherlands, 2004. Elsevier Science.

[16] M.W. Farthing and C. T. Miller. A comparison of high-resolution, finite-volume, adaptive-stencil schemes for simulating advective-dispersive transport. *Advances in Water Resources*, 24(1):29–48, 2000.

[17] R. W. Healy and T. F. Russell. A finite-volume Eulerian-Lagrangian localized adjoint method for solution of the advection-dispersion equation. *Water Resources Research*, 29(7):2399–2413, 1993.

[18] R. W. Healy and T. F. Russell. Solution of the advection-dispersion equation in two dimensions by a finite-volume Eulerian-Lagrangian localized adjoint method. *Advances in Water Resources*, 21:11–26, 1998.

[19] H. Holden and N.H. Risebro. *Front Tracking for Hyperbolic Conservation Laws*. Springer-Verlag, New York, NY, 2002.

[20] J. F. Kanney, C. T. Miller, and D. A. Barry. Comparison of fully coupled approaches for approximating nonlinear transport and reaction problems. *Advances in Water Resources*, 26(4):353–372, 2003.

[21] K. Hvistendahl Karlsen, K.-A. Lie, N.H. Risebro, and J. Frøyen. A front tracking approach to a two-phase fluid flow model with capillary forces. *In Situ*, 22(1):59–89, 1998.

[22] C. T. Kelley. *Iterative Methods for Linear and Nonlinear Equations*. Society for Industrial and Applied Mathematics, Philadelphia, 1995.

[23] P. Knabner, J.W. Barrett, and H. Kappmeier. Lagrange-Galerkin approximation for advection-dominated nonlinear contaminant transport in porous media. In A Peters, G. Wittum, B. Herrling, U. Meissner, C.A. Brebbia, W.G. Gray, and G.F. Pinder, editors, *Computational Methods in Water Resources X*, volume 1, pages 299–307, Norwell, MA, 1994. Kluwer Academic.

[24] P. Knabner, H. Kappmeier, and J.W. Barrett. Lagrange-Galerkin approximation for advection-dominated contaminant transport with nonlinear equilibrium or non-equilibrium adsorption. In R. Helmig, W. Jäger, W. Kinzelbach, and P. Knabner, editors, *Modeling and Computation in Environmental Sciences*, volume 59 of *Notes on Numerical Fluid Mechanics*, pages 36–48, Braunschweig, Germany, 1997. Vieweg Verlag.

[25] D. Kuzmin and S. Turek. Flux correction tools for finite elements. *Journal of Computational Physics*, 175:525–558, 2002.

[26] J.O. Langseth. On an implementation of a front tracking method for hyperbolic conservation laws. *Advances in Engineering Software*, 26:45–63, 1996.

[27] R. J. LeVeque. *Numerical Methods for Conservation Laws*. Birkhäuser Verlag, Boston, MA, 1992.

[28] C. T. Miller, G. Christakos, P. T. Imhoff, J. F. McBride, J. A. Pedit, and J. A. Trangenstein. Multiphase flow and transport modeling in heterogeneous porous media: Challenges and approaches. *Advances in Water Resources*, 21(2):77–120, 1998.

[29] K.W. Morton, A. Priestley, and E. Süli. Stability of the Lagrange-Galerkin method with non-exact integration. *Mathematical Modelling and Numerical Analysis*, 22(4):625–653, 1988.

[30] N.H. Risebro and A. Tveito. A front tracking method for conservation

laws in one dimension. *Journal of Computational Physics*, 101:130–139, 1992.

[31] T. F. Russell and M.A Celia. An overview of research on Eulerian-Lagrangian localized adjoint methods (ELLAM). *Advances in Water Resources*, 25:1215–1231, 2002.

[32] T. F. Russell, C.I. Heberton, L.F. Konikow, and G.Z. Hornberger. A finite-volume ELLAM for three-dimensional solute-transport modeling. *Ground Water*, 41(2):258–272, 2003.

[33] T.F. Russell. Eulerian-Lagrangian localized adjoint methods for advection-dominated problems. In D.F. Griffiths and G.A. Watson, editors, *Numerical Analysis 1989*, volume 228 of *Pitman Research Notes in Mathematics Series*, pages 206–228, Harlow, UK, 1990. Longman Scientific and Technical.

[34] T.F. Russell and P. Binning. Oh no, not the wiggles again! a revisit of an old problem and a new approach. In C.T. Miller, M.W. Farthing, W.G. Gray, and G.F. Pinder, editors, *Computational Methods in Water Resources XV*, volume 1, pages 483–495, Amsterdam, The Netherlands, 2004. Elsevier Science.

[35] J.E. Våg, H. Wang, and H.K. Dahle. Eulerian-lagrangian localized adjoint methods for systems of nonlinear advective-diffusive-reactive transport equations. *Advances in Water Resources*, 19(5):297–315, 1996.

[36] C.J. van Duijn and P. Knabner. Solute transport in porous-media with equilibrium and nonequilibrium multiple-site adsorption – traveling waves. *Journal Für Die Reine Und Angewandte Mathematik*, 415: 1–49, 1991.

[37] C.J. van Duijn and P. Knabner. Travelling waves in the transport of reactive solutes through porous-media – adsorption and binary ion-exchange.

1. *Transport in Porous Media*, 8(2):167–194, 1992.

[38] C.J. van Duijn and P. Knabner. Travelling waves in the transport of reactive solutes through porous-media – adsorption and binary ion-exchange. 2. *Transport in Porous Media*, 8(3):199–225, 1992.

[39] H. Wang, M. Al-Lawatia, and R.C. Sharpley. A characteristic domain decomposition and space-time local refinement method for first-order linear hyperbolic equations with interfaces. *Numerical Methods for Partial Differential Equations*, 15:1–28, January 1999.

[40] H. Wang, H.K. Dahle, R.E. Ewing, M.S. Espedal, R.C. Sharpley, and S. Man. An ELLAM scheme for advection-diffusion equations in two dimensions. *SIAM Journal on Scientific Computing*, 20:2160–2194, 1999.

[41] H. Wang, R.E. Ewing, and M.A. Celia. Eulerian-Lagrangian localized adjoint methods for reactive transport with biodegradation. *Numerical Methods for partial differential equations*, 11:229–254, 1995.

[42] H. Wang, W. Zhao, M.S. Espedal, and A.S. Telyakovskiy. An Eulerian-Lagrangian localized adjoint method for compositional multiphase flow in the subsurface. In C.T. Miller, M.W. Farthing, W.G. Gray, and G.F. Pinder, editors, *Computational Methods in Water Resources XV*, volume 1, pages 495–504, Amsterdam, The Netherlands, 2004. Elsevier Science.

[43] A. Younes. An accurate moving grid Eulerian Lagrangian localized adjoint method for solving the one-dimensional variable-coefficient ADE. *International Journal for Numerical Methods in Fluids*, 45:157–178, 2004.

[44] A. Younes, F. Lehmann, and Ph. Ackerer. A moving grid Eulerian Lagrangian localized adjoint method for solving linear and nonlinear advection-diffusion-reaction equations. In C.T. Miller, M.W. Farthing, W.G. Gray, and G.F. Pinder, editors, *Computational Methods in Water Resources XV*, volume 1, pages 519–530, Amsterdam, The Netherlands,

2004. Elsevier Science.

CENTER FOR COMPUTATIONAL MATHEMATICS REPORTS

University of Colorado at Denver
P.O. Box 173364, Campus Box 170
Denver, CO 80217-3364

Fax: (303) 556-8550
Phone: (303) 556-8442
http://www-math.cudenver.edu/ccm

192. Jan Mandel, "Iterative Substructuring with Lagrange Multipliers for Coupled Fluid-Solid Scattering,", August 2002.
193. D. W. Dean, "On the Estimation Of Diffusion Process Parameters From Time Series Data," September 2002.
194. Jan Mandel and Clark R. Dohrmann, "Convergence of a Balancing Domain Decomposition by Constraints and Energy Minimization," November 2002.
195. Kenneth D. Jarman and Thomas F. Russell, "Eulerian Moment Equations for 2-D Stochastic Immiscible Flow," January, 2003.
196. Cidalia Costa Fonte and Weldon A. Lodwick, "Areas of Fuzzy Geographic Entities", March, 2003.
197. Anatolii Puhalski, "On the Giant Component of the Sparse Random Graph, March, 2003.
198. Lucia Catabriga, Alvaro L. G. A. Coutinho, and Leopoldo P. Franca, "Evaluating the LCD Algorithm for Solving Linear Systems of Equations Arising from Implicit SUPG Formulation of Compressible Flows," May, 2003.
199. Leopoldo P. Franca and Saulo P. Oliveira, "Resolving Boundary Layers with the Discontinuous Enrichment Method," May, 2003
200. Craig J. Johns and Robert H. Shumway, "A Nonlinear and Non-Gaussian State-Space Model for Censored Air Pollution Data," May 2003.
201. Andrew V. Knyazev, "Analysis of transmission problems on Lipschitz boundaries in stronger norms," July 2003.
202. Lynn S. Bennethum and Tessa Weinstein, "Three Pressures in Porous Media, Updated," July 2003.
203. R. A. Klausen and T. F. Russell, "Relationships Among Some Locally Conservative Discretization Methods Which Handle Discontinuous Coefficients," July 2003.
204. K. David Jamison, Weldon A. Lodwick and Guerin Olsen, "A Method for Finding an Optimal Investment and Distribution Strategy for an Individual Retiree," October, 2003.
205. Thomas F. Russell and Phillip Binning, "Oh No, not the Wiggles Again! A Revisit of an Old Problem and a New Approach," March 2004.